

# **Microstructure-Texture Evolution Studies on IMI 834 Titanium Alloy during High Pressure Torsion**

June 2015

***Mr. Sushil Gyanoba Yebaji***

M. Tech. Scholar

Roll No. MS13M1008

Supervisor: Dr. Suhash Ranjan DEY



भारतीय प्रौद्योगिकी संस्थान हैदराबाद  
Indian Institute of Technology Hyderabad

*Research proposal submitted to the*  
Department of Materials Science and Metallurgical Engineering  
Indian Institute of Technology, Hyderabad  
Ordnance Factory Estate, Yeddumailaram -502205

## Declaration

I declare that this written submission represents my ideas in my own words, and where others' ideas or words have been included, I have adequately cited and referenced the original sources. I also declare that I have adhered to all principles of academic honesty and integrity and have not misrepresented or fabricated or falsified any idea/data/fact/source in my submission. I understand that any violation of the above will be a cause for disciplinary action by the Institute and can also evoke penal action from the sources that have thus not been properly cited, or from whom proper permission has not been taken when needed.



(Signature)

SUSHIL YEBAJI

(Sushil Yebaji)

MS13M1008.

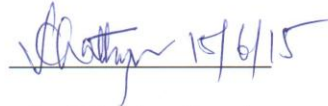
(Roll No: ms13m1008)

## Approval Sheet


This thesis entitled Microstructure-Texture Evolution Studies on IMI 834 Titanium Alloy during High Pressure Torsion by Sushil Yebaji is approved for the degree of Master of Technology from IIT Hyderabad.

  
15.6.2015

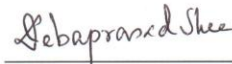
Dr. Bharat Bhooshan Panigrahi  
(Department of Materials Science and Metallurgical Engineering)  
Examiner

  
15/6/15

Dr. Subhradeep Chatterjee  
(Department of Materials Science and Metallurgical Engineering)  
Examiner

  
S.R. Dey

Dr. Suhash Ranjan Dey  
(Department of Materials Science and Metallurgical Engineering)  
Adviser

  
Debaprasad Shee

Dr. Debaprasad Shee  
(Department of Chemical Engineering)  
Chairman

## Acknowledgements

The M.Tech course work at IIT Hyderabad was a great learning experience for me. The thesis work made me learn many new things and made me confident to work on the equipment and explore new ideas. This work would not have executed without the support of many people, who helped me in numerous ways.

I am highly obliged to my guide, Dr. Suhash Ranjan Dey, who deeply inspired me throughout this work. With his esteemed guidance and motivation only, I was able to successfully execute the goals for this work. Also, I am grateful to Dr. Amit Bhattacharjee, DMRL, Hyderabad for providing us IMI-834 sample, Dr. Tsuji; kyoto university, japan for processing the HPT specimens in his laboratory. I am also thankful to Mr. Mohit Joshi, kyoto university, japan for helping while HPT processing. I am thankful to IITH-JICA friendship program for allowing Dr. Suhash Ranjan Dey to carry and process HPT on samples in japan. My great thank to Mr. BasanthKumar kodli and Mr. G. Dan Sathiaraj for helping me to conduct experiments and developing my skills to work on intricate equipment single handedly.

I would like to thank all faculty members and PhD scholars of Department of Material Science and Metallurgical Engineering for their constant guidance. Also, big thank to my M.Tech colleagues for helping me in course work and spending a great time together.

Lastly, my special gratitude to my parents, Mrs. Sangita Yebaji and Mr. Gyanoba Yebaji and my brother Mr. Akshay Yebaji for their love, guidance and blessings.

## Abstract

IMI 834 titanium alloy is a near  $\alpha$  (HCP) titanium alloy used for high temperature applications with the operating temperature up to 600°C. This alloy is extensively used in gas turbine engines such as high pressure compressor and low compressor discs, having desired with better dwell fatigue life and creep properties. These desired properties demands ultrafine grain microstructure with random crystallographic orientations i.e. random texture.

The  $\alpha$  phase, being limited by lesser number of possible crystallographic slip systems, upon conventional deformation generates strong texture. On the other hand severe plastic deformation (SPD) imparts large plastic strain without change of sample size and can generate ultra-fine grained microstructure, in turn imparting higher material strength and may generate random texture.

The present work deals with the high pressure torsion (HPT), a severe plastic deformation technique, of IMI 834 titanium alloy at various plastic strains (through rotations of 30°, 60°, 90°, 180° and one complete rotation) and then study of its microstructure-texture evolution. The hardness profile of the HPT samples provided its mechanical properties and the orientation maps (obtained through electron back-scattered diffraction technique) with crystallographic texture and grain boundary details generated its microstructure evolution details.

The hardness profile from center towards the edge of the HPT disc of various rotations shows hardening with increase in rotation, before finally reaching a saturation. At strains ( $\epsilon=0.79, 1.4$  and  $2.98$ ) softening with decreased hardness value is noticed.

The observed microstructural features indicated strong shear deformation along the hexagonal slip systems with continuous rotation (up to maximum 30°) of shear texture components mostly around  $\langle 10\bar{1}0 \rangle$  axis. Increased strain activated shear along  $\langle c+a \rangle$  generating C fibre and less probable pyramidal and prismatic shear along  $\langle a \rangle$  creating P fibre (movement of B towards P1 via Y). Also, with increased strain, deformation-partial dynamic recovery-deformation cycle is observed. Dynamic recovered strain microstructures (at  $\epsilon=1.4$  and  $2.98$ ) showed the reappearance of B fibre stating basal orientation i.e.  $(0002)\langle 11\bar{2}0 \rangle$  of the recovered grains.

Through HPT of IMI 834 alloy the initial material grain size ( $6 \mu\text{m}$ ) is reduced to ultrafine grain ( $1.8 \mu\text{m}$  at  $\epsilon=1.23$ ) in the fully deformed microstructure and to bimodal microstructure ( $1.3 \mu\text{m}$  and  $4.7 \mu\text{m}$  at  $\epsilon=2.98$ ) at the recovery stage.

**Keywords:** IMI 834 Titanium alloys, HPT- high pressure torsion, microtexture, ultrafine grain, dynamic recovery.

**SUSHIL YEBAJI**

**2, 3 SUSHILSHREE, 45/2A,  
SADASHIV NAGAR, HANDEWADI  
ROAD, HADAPSAR, PUNE,  
MAHARASHTRA-411028  
E-mail: [sushilyebaji@gmail.com](mailto:sushilyebaji@gmail.com)**

---

**Educational Qualifications:**

Pursuing M.Tech. from Indian Institute of Technology Hyderabad.

<b>Degree/ Examination</b>	<b>Year of Passing</b>	<b>School/Institute</b>	<b>Percentage of marks</b>
M.Tech. Materials Science and Metallurgical Engineering	2015	IIT HYDERABAD	9.58 (CGPA) till now
B. Tech. Metallurgical Engineering	2012	Pune University	6.49
H.S.C	2008	R R Shinde Jr College, Pune	81.75
S.S.C	2006	Sadhana Vidyalaya, Pune	91.4

**M. Tech. (Course work):**

- Advanced Physical Metallurgy
- Powder Metallurgy Manufacturing
- Properties of Materials
- Materials Synthesis and Characterization
- Electron Microscopy
- Fundamentals of Crystallographic Texture
- Introduction to Computational Methods in Materials Science
- Phase Transformations of Metals and Alloys
- Dislocation Theory for Mechanical Behaviour of Metals

**Project Profile:**

**B.Tech.:** *Material selection, die design for fabrication of polyvinyl chloride-copper composites & characterizing mechanical properties*

**Personal Details:**

- Date of Birth : 8<sup>th</sup> March 1991
- Linguistic Proficiency : English, Hindi, Marathi

# Contents

## 1. Introduction

1.1. Titanium and its conventional alloys.....	1
1.2. Development history of $\alpha$ /near- $\alpha$ conventional titanium alloys.....	1
1.3. High Pressure Torsion Processing.....	5

## 2. Literature Review

2.1. Deformation in Hexagonal Crystal.....	8
2.2. Evolution of hardness during HPT processing.....	10
2.3. Evolution of microstructure and texture during HPT processing .....	12
2.4. Objectives of the M.Tech Thesis .....	16

## 3. Experimental Procedures

3.1. Preparation of disks for HPT.....	17
3.2. High Pressure Torsion Processing.....	17
3.3. Characterization.....	19
3.3.1. Hardness test of processed HPT disks.....	19
3.3.2. Microstructure and Texture Characterization .....	19

## 4. Results

4.1. HPT processed specimens.....	21
4.2. Microhardness Properties.....	21
4.3. Microstructure Evolution.....	23
4.4. Microtexture Evolution.....	29

5. Conclusions.....	36
---------------------	----

References .....	37
------------------	----

# Chapter 1

## Introduction

### 1.1. Titanium and its conventional alloys:

Titanium is a chemical element found in group IV B in the transition metal series of the periodic table. Properties of Titanium such as light weight, high specific strength, excellent corrosion resistance and superior biocompatibility made it an attractive material in a wide variety of applications. Conventional titanium alloys are mainly classified into three categories such as  $\alpha$ /near- $\alpha$  alloys,  $\alpha+\beta$  alloys and  $\beta$  alloys depending on their stabilizing elements and thermo-mechanical processing. The commercially pure titanium of different grades and those with additions of  $\alpha$ -stabilizers such as aluminium, oxygen, nitrogen and carbon belong to  $\alpha$  titanium alloys. Alloys with 5-10% volume fraction of  $\beta$  phase consisting of 1-2%  $\beta$  stabilizers (Nb, Ta, V, Hf, etc.) are termed as near- $\alpha$  alloys. Further addition of  $\beta$  stabilizers increases the volume fraction of  $\beta$  phase up to 10-30% in the microstructure is known as  $\alpha+\beta$  alloys. Metastable  $\beta$  titanium alloys having higher concentration of  $\beta$  stabilizers resulting in retaining 100%  $\beta$  phase by fast cooling is called  $\beta$  alloys [1].

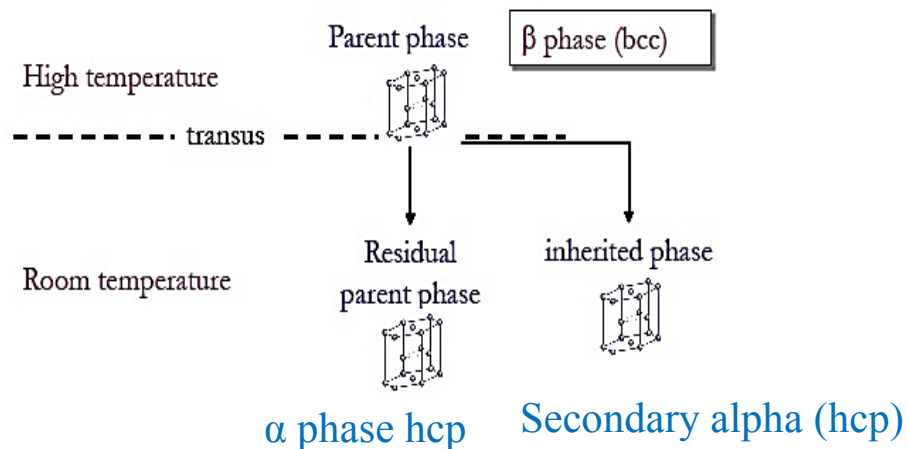


**Fig. 1.1** phases of titanium at room pressure [1].

### 1.2. Development history of $\alpha$ /near- $\alpha$ conventional titanium alloys:

Titanium alloys are excellent candidates for aerospace applications owing to their high strength to weight ratio and high corrosion resistance due to the formation of passive oxide surface film. Primary reasons for using  $\alpha$ /near- $\alpha$  conventional titanium alloys in the aerospace industry are: weight savings,



operating temperature, corrosion resistance and better thermal expansion compatibility of the composite [2].

Imperial Metal Industries (IMI) developed high temperature near- $\alpha$  titanium alloy named as IMI 834 with combination of elements as shown in Table No.1. The Ti alloy IMI 834 is one of the advanced additions to the list of the high temperature near- $\alpha$  conventional titanium alloys with high specific strength, developed as a substitute for the heavy nickel base super alloys. This is mainly used as compressor discs and blades in the advanced gas turbine jet engines with application temperature of 600°C. IMI 834 was used for compressor discs in the last two stages of the intermediate pressure compressor, and the first four stages of the high pressure compressor [3-4]. Similar composition of near- $\alpha$  titanium alloys was developed by another company (TIMETAL 834) and has been used for applications such as disks and blades in the high pressure part of aero engine compressors due to their excellent combination of creep and fatigue properties at working temperatures up to 600°C [5-7].

**Table 1.1:** Nominal composition of alloy IMI-834.

Ti	Al	Sn	Zr	Nb	Si	V	C	Mn
Balanced	6.30	3.84	3.71	0.54	0.32	0.11	0.08	0.04

In case of gas turbine engine the discs and blades are subjected to loading and unloading at the time of take-off and landing stages of each flight. This loading and unloading pattern with holding (dwelling) for certain time is called dwell cycling. As compared to low cycle fatigue (LCF) (without holding time), this alloy shows early failure due to deviation loading as well as failure characteristics [8]. Good creep properties are also required because of dwell period leads increase in operating temperature than low cycle fatigue (LCF). This problem can be overcome mainly by increasing volume percentage of  $\beta$  phase or by increasing the degree of random microtexture with fine grain microstructure.

IMI 834 Titanium alloy shows bimodal microstructure Fig. 1.2 shows combination of primary  $\alpha$  grains ( $\alpha_p$ ) and secondary  $\alpha$  colonies ( $\alpha_s$ ) which is called as bimodal microstructure. This bimodal microstructure consists of 45% of equiaxed primary  $\alpha$  grains ( $\alpha_p$ ) surrounded by 55% of Widmanstatten secondary  $\alpha$  colonies ( $\alpha_s$ ).

As per Fig. 1.3, when IMI-834 alloy subjected to loading crack mainly initiates in those primary  $\alpha$  grains which have slip plane orientation 45° loading axis and advances through secondary  $\alpha$  grains having minimum misorientation with respect to primary ones.

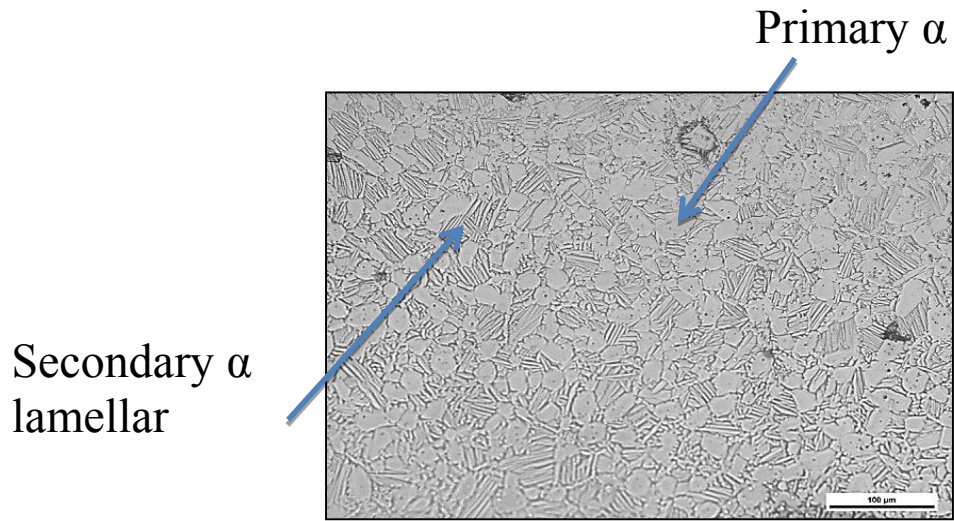


**Fig. 1.2** Optical micrograph of as received IMI-834 sample.

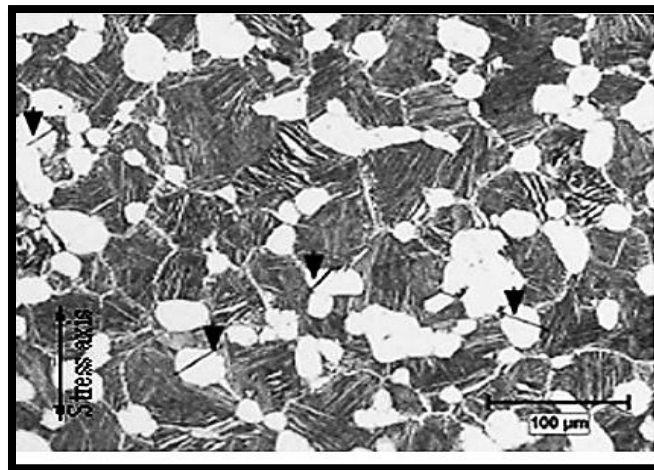


**Fig. 1.3** Optical microstructure of a dwell fatigue sample showing cracks (arrowed) in primary  $\alpha$  grains in relation to the orientations of  $\alpha$  platelets in transformed  $\beta$  grains, stress axis being vertical [8].

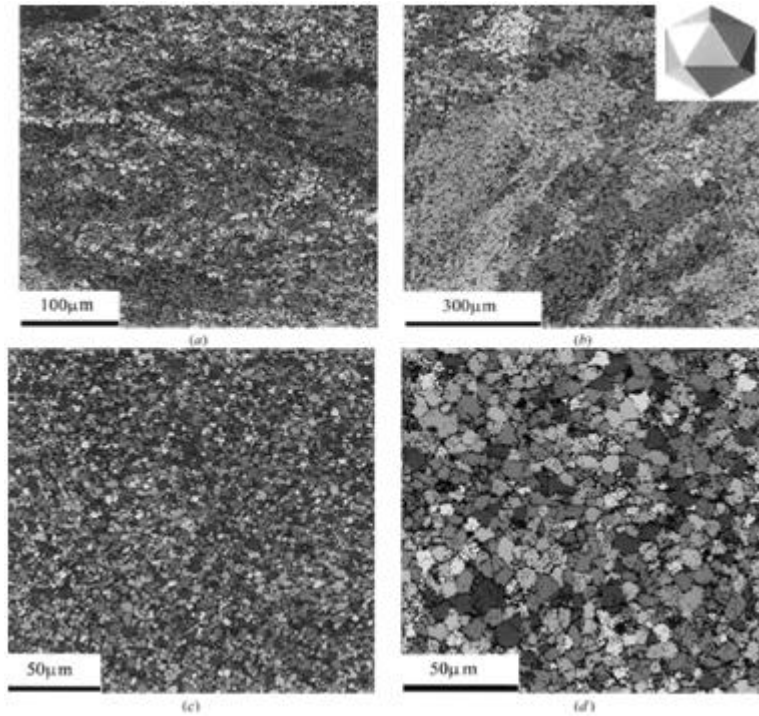


**Fig.1.4** Icosahedral images generated from EBSD analysis of Ti6242 in the following conditions: **(a)** conventional billet **(b)** conventional forging  
**(c)** Ultra-fine grain billet and **(d)** forged ultrafine grained billet.  
 Orientation to color relation is shown in upper right corner of (b) [10].

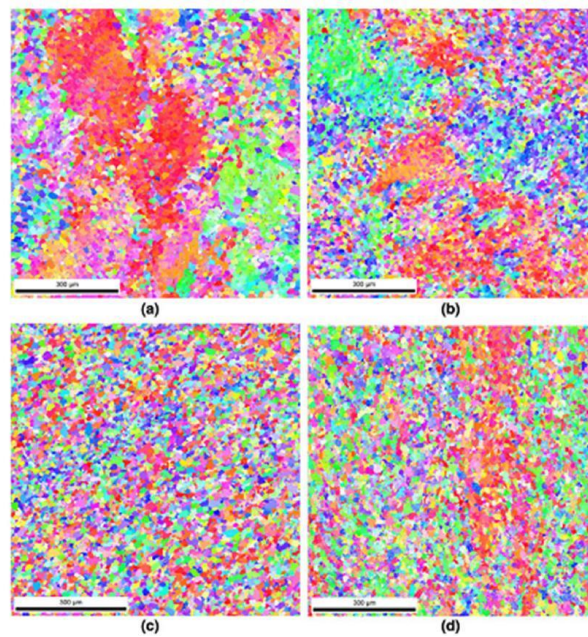


**Fig. 1.5** Representative tiles from larger EBSD scans of **(a)** sample 1, **(b)** sample 2, **(c)** sample 3, and **(d)** sample 4. The incident ultrasonic wave traverses from left to right in the images [11].

G.A. Salishchev et.al. performed thermomechanical processing of Ti6242 alloy in  $\alpha+\beta$  temperature range involving dynamic recrystallization to achieve uniform fine grain (UFG)  $\alpha$  titanium particles having homogeneous texture and prevent colony formation [9]. Gigliottiet. al. [10] investigated the textured colonies in Ti6242 alloys obtained through four conditions which includes conventional billet, conventional  $\alpha+\beta$  forging, ultrafine grain (UFG) billet and an  $\alpha+\beta$  forging made from the ultrafine grain billet through ultrasonic attenuation technique and SEM-EBSP method. These four different products forms alternative degrees of microtexture stages as detected from EBSP analysis shown in Fig. 1.4. The EBSP results showed that free forged ultrafine grained billet i.e. Fig. 1.4(c) contains no micro texture.

A. Bhattacharjeet. al. [11] investigated the textured colonies in Ti6242 alloys obtained through four different  $\alpha+\beta$  forging conditions. These four different samples forms alternative degrees of microtexture regions as detected from EBSP analysis shown in Fig. 1.5. Fig. 1.5(c) contains random distribution of orientations and it is free from microtexture and henceforth is desired.

There are mainly two ways to achieve random distribution of orientations (random crystallographic texture):

- Forging in  $\beta$  phase (i.e. through dynamic recrystallization of the  $\beta$  phase) or
- Severe plastic deformation of  $\alpha$  phase

In this M.Tech. thesis research, the author has tried to perform severe plastic deformation (HPT) on the  $\alpha$  phase and then study its microstructure-texture evolution.

### **1.3 High Pressure Torsion Processing (HPT)**

Fabrication of ultrafine grains can be achieved by two methods: bottom up technique or top down approach.

Bottom-up fabrication is performed through synthesis and consolidation individual atoms or nano-particles solids, such as, electro deposition [12], inert gas condensation [13] and ball milling followed by subsequent consolidation [14]. Despite the fact that these methods have the capability to produce very small grain size, they suffer from disadvantages such as small size of the finished product, often residual porosity.

The “top-down” approach involves a bulk solid having relatively coarse grain size, processed to produce a UFG microstructure through heavy straining. This approach avoids the small product sizes, defects like porosity and the contamination which are inherent features of materials produced using the “bottom-up” approach and it has the additional advantage that it can be readily applied to a wide range of

pre-selected alloys. In order to convert a coarse-grained solid into a material with ultrafine grains, it is necessary to impose an exceptionally high strain in order to introduce a high density of dislocations and for these dislocations to subsequently re-arrange to form an array of grain boundaries [15].

Severe Plastic Deformation (SPD) is the most well-known top down approach for fabrication UFG materials. Fabrication of materials by SPD is usually done by imposing very high plastic strain, without concomitant changes in the dimensions of the work pieces. SPD techniques such as Equi-Channel Angular Processing (ECAP) (Fig 1.6a) [16], Accumulative Roll Bonding (ARB) (Fig 1.6b) [17] and High Pressure Torsion (HPT) (Fig 1.6c) [18] can now successfully produce wide variety of bulk ultrafine grained materials. The disadvantages associated with Bottom-up approach may be completely overcome in Top-down approach in which bulk solid with coarse grain size is processed by imposing high strain in order to refine the grain size to sub-micrometer size.

Amongst various SPD processing techniques, HPT has gained significant attention due to fact that large plastic strain value can be easily achieved in this process. The sample in the form of thin disc is placed between two anvils and a very high compressive load is applied with simultaneous torsion strain (Fig 1.6c). Successive twisting while application of compressive loading leads to higher shearing strain as compared to normal work-hardening techniques helping in achieving UFG.

The pioneering works by Bridgman lead to the origin of metals processing by HPT [18]. Prof. Bridgman won Nobel Prize in Physics for his extensive research on Physics of High Pressure.

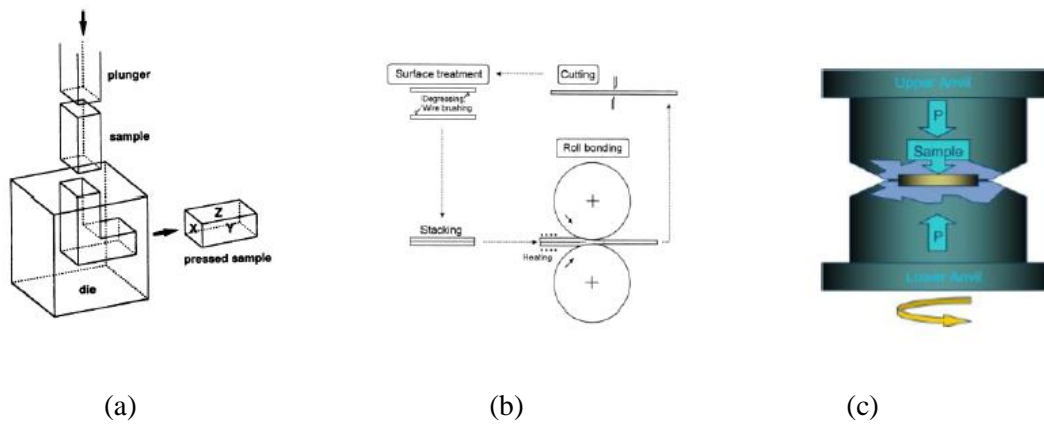


**Fig 1.6:** S.P.D processes (a) ECAP [16], (b) ARB [17] and (c) HPT [18].

The equivalent strain value in HPT can be calculated by:

$$\epsilon \approx \frac{1}{\sqrt{3}} \frac{r}{h} \varphi$$

Where  $r$  = radius of the disc in mm,  $h$  = height of disc in mm,  
 $\varphi$  = angle of rotation in radians and  $\epsilon$  = equivalent strain value.

According to the equation the strain is directly proportional to the radius of the disc which indicates that at the center the strain is ideally zero whereas the strain is highest at the edges of the disc.

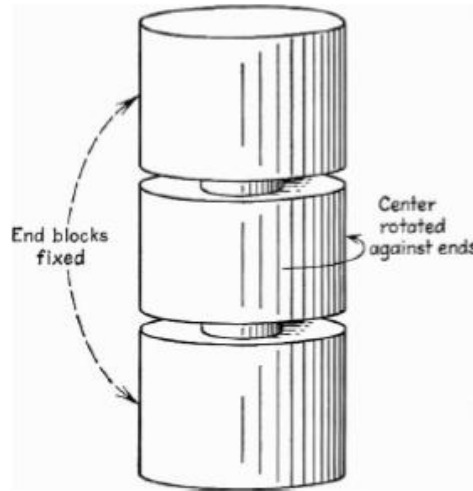


**Fig 1.7** General schematic of the apparatus used by Bridgman in which torsional straining is combined with longitudinal compression [18].

Extensive research has been conducted on various alloys to investigate the effect of HPT on the evolution of microstructure and mechanical properties [19-21]. The investigations on the HPT processing indicate that there is increase in the hardness with the increase in the strain or the number of rotations and at high strain values, the hardness homogeneity is achieved. It is generally observed that HPT processing leads to development of ultrafine grains at high strain levels separated by high angle grain boundaries (HAGBs).



## Chapter 2

### Literature Review

#### 2.1 Deformation in Hexagonal Crystal

Deformation in hexagonal crystal is achieved through dislocation glides in five crystallographic slip systems (mentioned below and are also shown in Fig. 2.1) and/or through twinning.

- |              |                                 |                                               |
|--------------|---------------------------------|-----------------------------------------------|
| 1. Basal     | $\langle a \rangle$             | $\{0001\} \langle 11\bar{2}0 \rangle$ ,       |
| 2. Prismatic | $\langle a \rangle$             | $\{1\bar{1}00\} \langle 11\bar{2}0 \rangle$ , |
| 3. Pyramidal | $\langle a \rangle$             | $\{10\bar{1}1\} \langle 11\bar{2}0 \rangle$ , |
| 4. Pyramidal | $\langle c + a \rangle$ type I  | $\{10\bar{1}1\} \langle 11\bar{2}3 \rangle$ , |
| 5. Pyramidal | $\langle c + a \rangle$ type II | $\{11\bar{2}2\} \langle 11\bar{2}3 \rangle$ . |

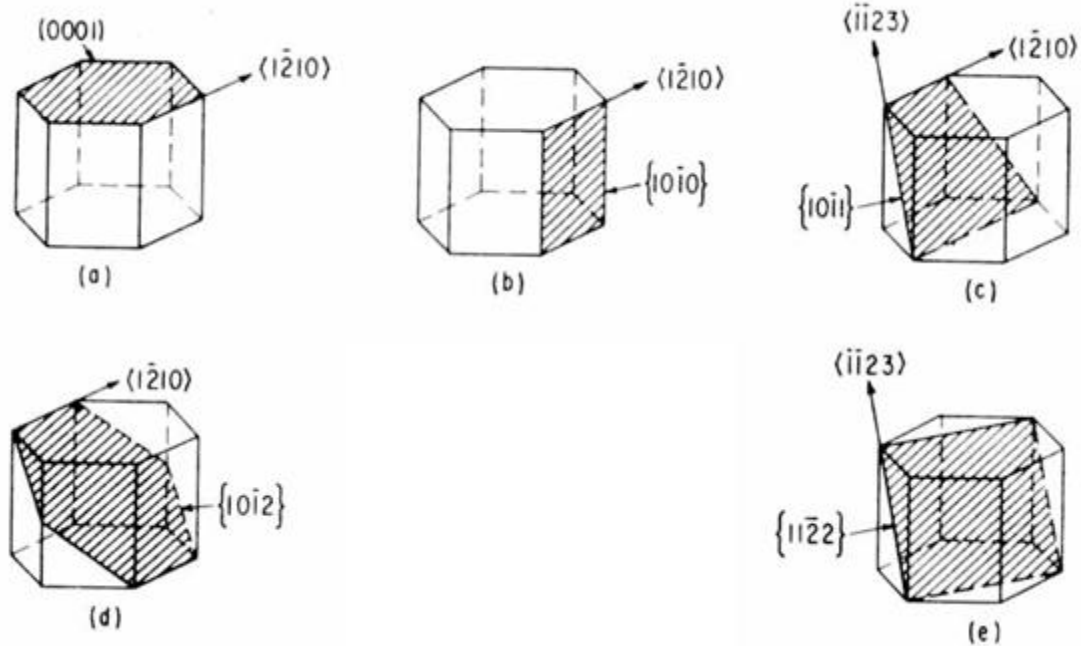


**Fig 2.1** The planes and directions that are considerable as possible slip systems:

- (a) Basal slip  $\{0001\} \langle 1\bar{2}10 \rangle$  (b) Prismatic  $\langle a \rangle$  slips  $\{10\bar{1}0\} \langle 1\bar{2}10 \rangle$   
(c) Pyramidal  $\langle a \rangle$  slips  $\{10\bar{1}1\} \langle 1\bar{2}10 \rangle$  (d) Pyramidal  $\langle c+a \rangle$  Type I slips  $\{10\bar{1}2\} \langle 1\bar{2}10 \rangle$   
(e) Pyramidal  $\langle c+a \rangle$  Type II slips  $\{11\bar{2}2\} \langle 1\bar{1}23 \rangle$  [22].

The activation of slip system during deformation varies in hexagonal materials. But generally basal slip is more favoured than prismatic/pyramidal  $\langle a \rangle$  slips and pyramidal  $\langle c+a \rangle$  slips.

HPT produces simple shear motions in the specimen and to analyse the shear components in the specimen, the crystallographic pole figures obtained from X-ray diffraction/electron backscatter diffraction are transformed into torsion  $Z$ - $\theta$  coordinates where  $Z$  denotes shear plane normal (SPN) and  $\theta$  denotes shear direction (SD). The standard torsion texture for HCP metal is shown in Fig. 2.2.

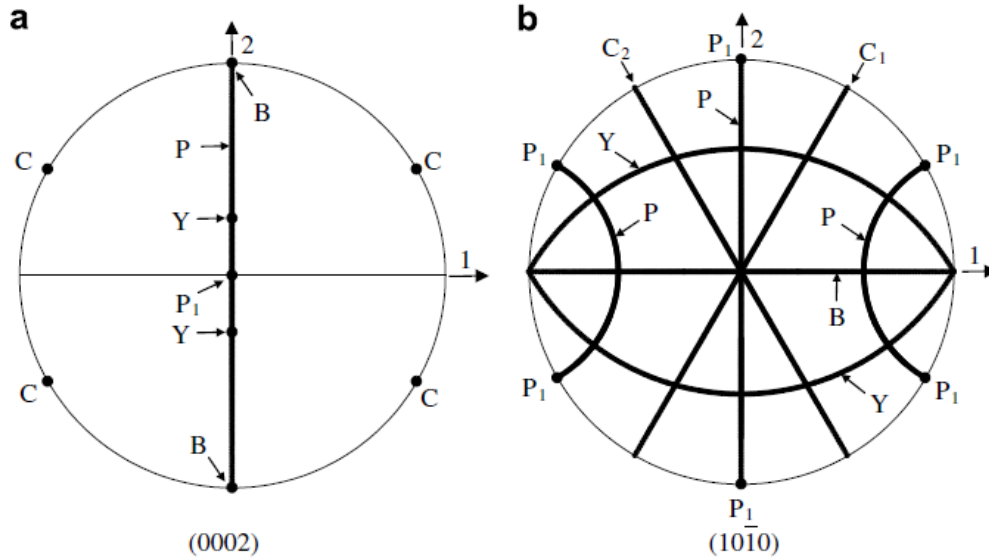


**Fig. 2.2** Ideal orientations of magnesium under simple shear as they appear in the (a) (0002) and (b)  $(10\bar{1}0)$  pole figures [19].

These pole-figures mainly consist of four fibres:

1. The B fibre ( $0^\circ, 90^\circ, 0-60^\circ$ ); basal plane  $\parallel$  shear plane.
2. The P fibre ( $0^\circ, 0-90^\circ, 30^\circ$ );  $\langle a \rangle \parallel$  shear direction. The end-orientation of this fibre is called P1, its appearance in the  $u = 0^\circ$  section is redundant along several lines for two reasons:
  - (i) Because of the singularity of Euler space at  $u = 0^\circ$ ;
  - (ii) It appears also at different locations because of the hexagonal crystal symmetry.
3. The Y fibre ( $0^\circ, 30^\circ, 0-60^\circ$ ); this is a 'c' fibre, meaning that the fibre axis is the c-axis which is rotated towards the shear plane by  $30^\circ$ .
4. The C1 fibre ( $60^\circ, 90^\circ, 0-60^\circ$ )
5. C2 fibre ( $120^\circ, 90^\circ, 0-60^\circ$ ); these are also 'c' fibres where the c-axis is first rotated  $90^\circ$  in the shear direction, then  $\pm 30^\circ$  in the shear plane direction.

Fig. 2.3 denotes relative activities of slip systems along four fibres, In basal fibre only basal slip system is activated, while in P fibre as  $\theta$  increases from  $0^\circ$  to  $90^\circ$ , activity of prismatic and pyramidal fibres decreases while activity of basal fibre increases continuously, in case of Y fibre activity of basal,



prismatic and pyramidal slip systems are almost same, but in  $C_1$ ,  $C_2$  fibres mainly consist pyramidal first order and pyramidal second order slips.

In hexagonal system, twinning also include in deformation system as deformation slips, which are given as follows [22]:

- Tension twins  $\{10\bar{1}2\}\langle 10\bar{1}1\rangle$  and  $\{11\bar{2}1\}\langle 11\bar{2}6\rangle$
- Compression twin  $\{11\bar{2}2\}\langle 11\bar{2}3\rangle$

Since twins are not noticed in the microstructure of the HPT IMI 834 alloy so they are not taken into account.

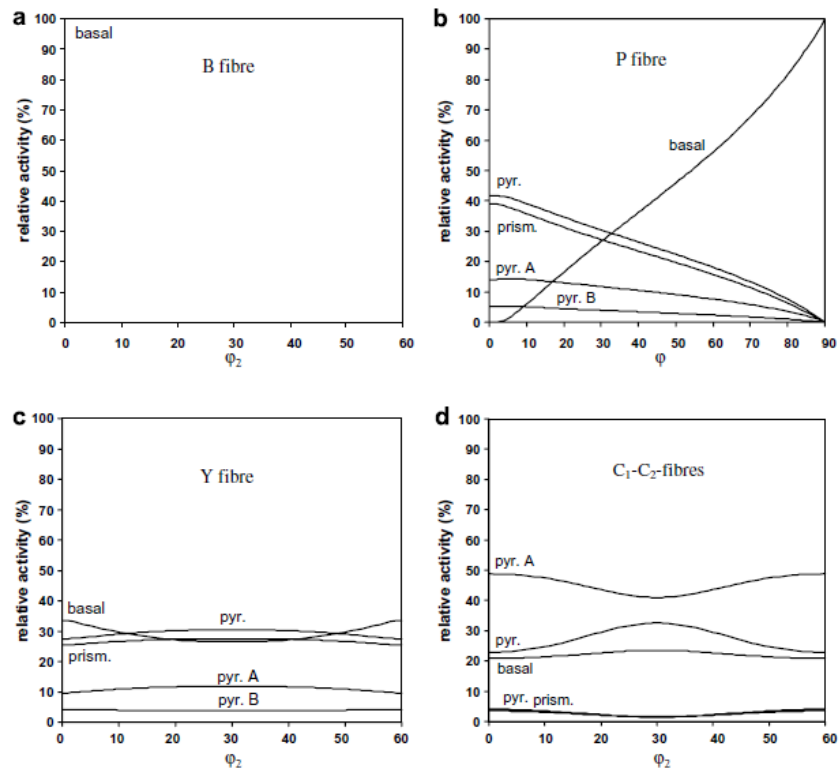


**Fig. 2.3** Relative slip activities of the slip system families for the set of reference stresses [1, 8, 8, 6, 6], along: **(a)** B fibre, **(b)** P fibre, **(c)** Y fibre and **(d)**  $C_1$ – $C_2$  fibres [21].

## 2.2 Evolution of hardness during HPT processing

Since strain introduced depends upon the distance from the center of the specimen and torsion rotation values so hardness is measured along both the radius and the strain values. Y.C. Wang et. al. [20] measured hardness on HPT processed two different heat treated Ti–6Al–4V alloys containing different volume fractions of  $\alpha$  structures (equiaxed  $\alpha$  grain and  $\alpha+\beta$  lath). Ti64-1 alloy contained 85% equiaxed  $\alpha$  grains and Ti64-2 alloy consisted of 48% equiaxed  $\alpha$  grains. Both materials were processed with HPT at

room temperature under an applied pressure of 6.0 GPa. Graph (Fig 2.4) shows microhardness values against equivalent strain and it tells increase in microhardness up to equivalent strain of  $\sim 20$  with subsequent stabilization at higher strains [20]. Decreasing equiaxed  $\alpha$  grains showed higher microhardness value. Also can be noticed in Fig 2.5 graph that higher straining brought homogeneity in the microhardness values.

Zhilaev et. al. [18] measured hardness values along the radius of CP aluminum processed with HPT at pressure of 1 GPa and is recorded in Fig. 2.6. Lower broken lines denote hardness values of annealed samples. The lower set of experimental points correspond to the samples with only applied pressure i.e. without any torsion ( $N = 0$ ). For  $N = 1$  revolution, sharp deviation in hardness values in center to edge is spotted which is higher than  $N = 0$ . Values of  $H_v$  in the central region increase with increasing numbers of revolutions. Samples of  $N = 4, 8$  reveals rational level of homogeneity across disks. So, Fig. 2.6 demonstrates that there is a sensible degree of macroscopic homogeneity across the disks when the numbers of revolutions equals or exceeds 4.

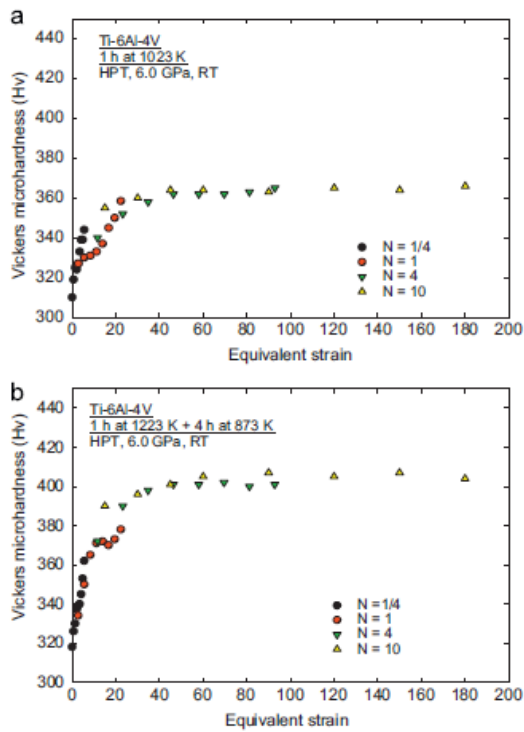


**Fig. 2.4** Values of the Vickers microhardness plotted against the equivalent strain for (a) Ti64-1 alloy and (b) Ti64-2 alloy [21].

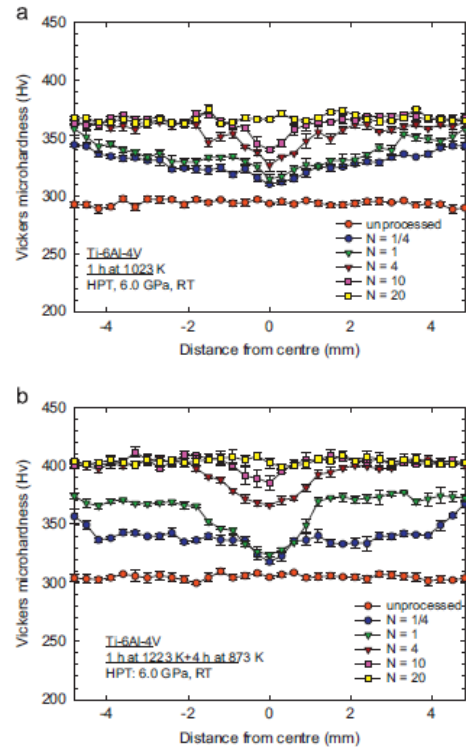


**Fig. 2.5** Values of the Vickers microhardness plotted against the positions on the disks for (a) Ti64-1 and (b) Ti64-2 [21].

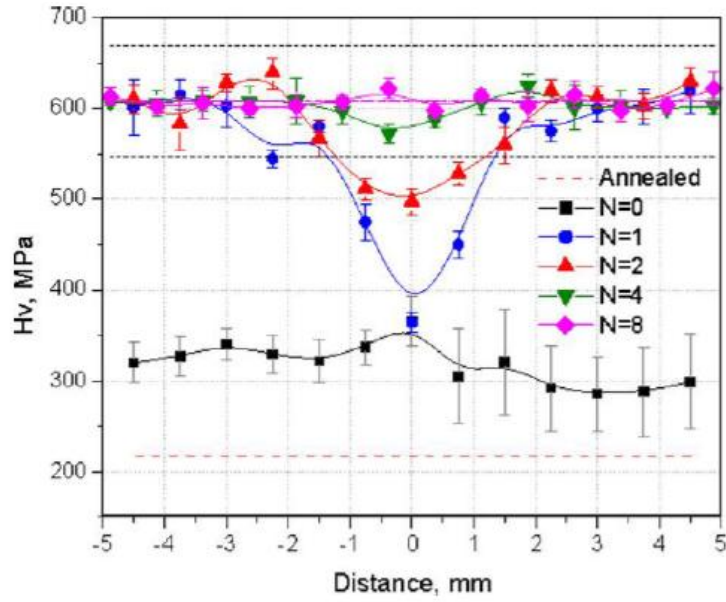


**Fig 2.6** Microhardness distributions across the diameters of aluminium discs subjected to HPT at a pressure of  $P=1\text{GPa}$  and up to eight turns [18].

### 2.3 Evolution of microstructure and texture during HPT processing

The microstructure and texture are the most important parameters for properties determination but only seldom their evolution is studied in details. Fig. 2.7 shows the graph between area fraction and grain size of HPT of Ti-6Al-4V alloys with different volume fraction of  $\alpha$  structures [20]. Undergoing grain refinement in the samples (Ti64-1 and Ti64-2 alloy), the measured equilibrium grain sizes after 20 turns are  $\sim 130\text{ nm}$  in Ti64-1 alloy and  $\sim 70\text{ nm}$  in Ti64-2 alloy.

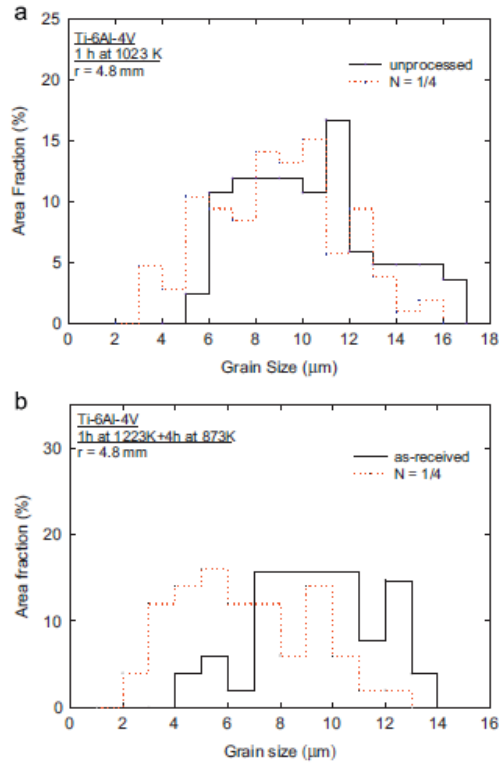


**Fig. 2.7** Distributions of grain sizes in the unprocessed condition and after 1/4 turn for (a) Ti64-1 alloy and (b) Ti64-2 alloy [20].

S. Biswas et. al. [21] studied the effect of HPT on magnesium at elevated temperature 250°C. Fig. 2.8 shows area and number fraction information about initial and heavily deformed (shear strain = 1.73) samples. On the basis of area fraction and number fraction of the grains, it can be easily noticed that the initial sample consisted of bimodal microstructure and the deformed microstructure is composed of small grains in large number, signifying grain refinement during the torsion process. In order to further analyse the microstructure refinement, the grains were partitioned between deformed grains and (presumably) dynamically recrystallized grains. The grain size distribution with a minimum of ~10 μm were considered to be dynamically recrystallized grains and those larger than 10 μm were taken to be deformed ones. With this partitioned data, the area fraction, shear direction and shear texture through pole figures with simulation results of the dynamically recrystallized and the deformed grains were studied (displayed in Fig. 2.9 and Fig. 2.10). It can be seen that the fraction of dynamically recrystallized grains increases with increase in strain. Almost half of the grains were dynamically recrystallized before fracture (at strain = 1.73).

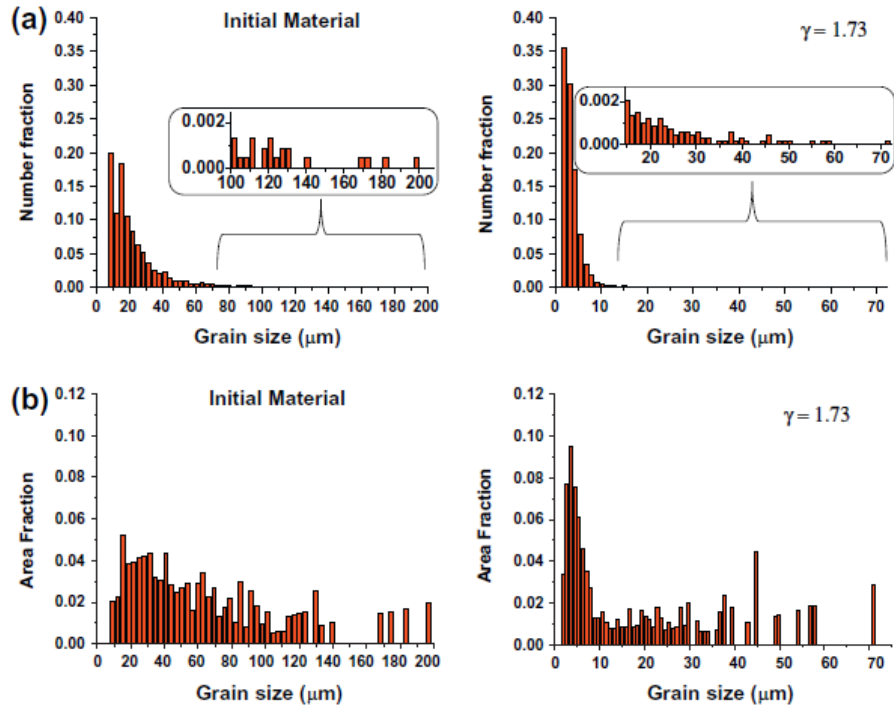


**Fig. 2.8** Grain size distribution for the starting material and at fracture of the torsion samples.

(a) Area fraction, (b) Number fraction [21].

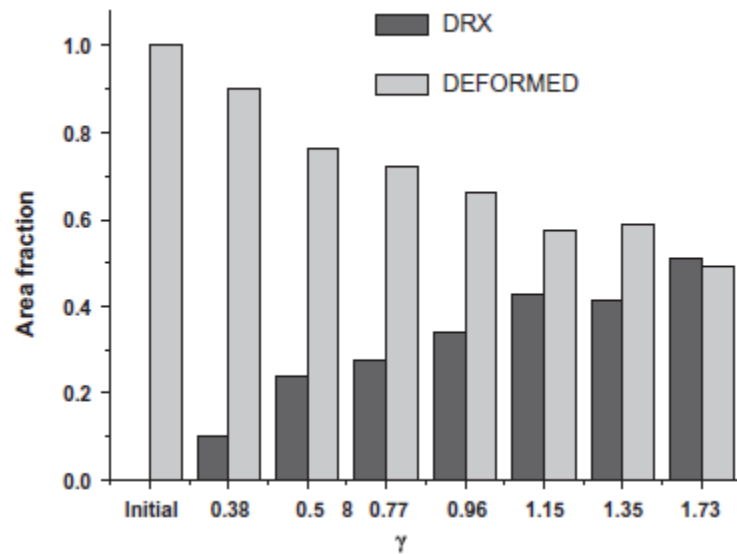


**Fig. 2.9** Area fraction of dynamically recrystallized grains and deformed grains as a function of shear strain [21].

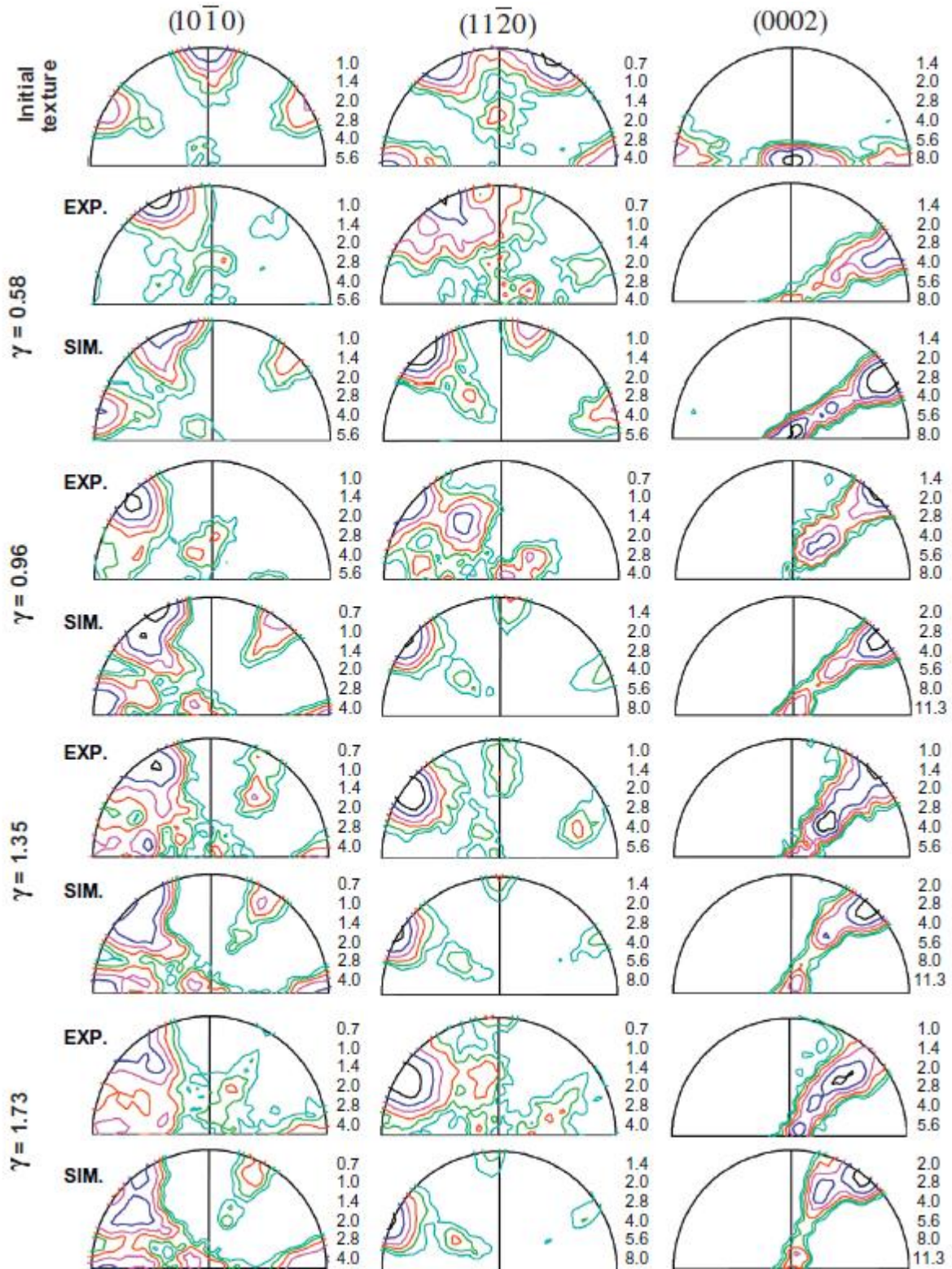


**Fig. 2.10**  $(10\bar{1}0)$ ,  $(11\bar{2}0)$  and  $(0002)$  pole figures as a function of strain obtained experimentally and by simulation (h on the right, Z at the top, with R being the projection plane) [21].



Fig. 2.10 displays  $(10\bar{1}0)$ ,  $(11\bar{2}0)$  and  $(0002)$  pole figures (experimental and simulation) in Z- $\Theta$  direction. The initial material shows  $\langle 10\bar{1}0 \rangle \parallel Z$  type partial fibre. At the same time, the c-axis is perpendicular to the longitudinal axis of the bar (see the  $(0002)$  pole figure). Generally, the main orientation for hcp materials subjected to simple shear (torsion) is the B fibre (see Fig. 2.2 for ideal orientations). Under applied shear there showed C and  $P_1$  fibre with a progressive anticlockwise rotation of the texture around the radial axis towards that of the B fibre. The deformation is simulated through simple shear in five hcp slip systems using viscoplastic self-consistent (VPSC) model with critical resolved shear stress values of 15 MPa for basal, 105 MPa for prismatic and pyramidal and 67 MPa for pyramidal type I and pyramidal type II slips and found to match with the experimentally obtained pole figures. There noticed no difference between deformed and dynamically recrystallized texture except grain refinement.

#### **2.4. Objectives of the Thesis**

IMI 834 alloys (a near  $\alpha$  titanium alloy) requires ultrafine grained random textured microstructure for better dwell fatigue life for its application. Severe plastic deformation is known to generate ultrafine grained microstructure. To study the effects of severe plastic deformation (carried out through high pressure torsion) on  $\alpha$  phase of IMI 834 alloy, the following objectives are addressed in this thesis:

- (1) Performing high pressure torsion of various rotations on IMI 834 to obtain different strain values;
- (2) Hardness profiling of the HPT deformed IMI 834 with respect to strain and distance from the center of the sample (along the radius);
- (3) Comprehensive microstructure-crystallographic texture characterization of the HPT deformed IMI 834 alloy at all strain values to understand the deformation mechanism and its evolution in obtaining the final ultrafine grained microstructure.

## Chapter 3

### Experimental Procedure

#### 3.1 Preparation of Disks for HPT

IMI 834 sample was received in the form of pan cake (dimensions: 250mm  $\varnothing$  and 12mm height). It was sliced as per desired dimensions i.e. 10mm $\varnothing$  by using EDM wire cutter experiment and 0.8mm height was achieved first by EDM cutter and then grinding specimen using SiC grit papers with grit size of 500, 1000, 1200 and 2000 respectively. The disks are then designated according to the number of rotations as per the given chart.

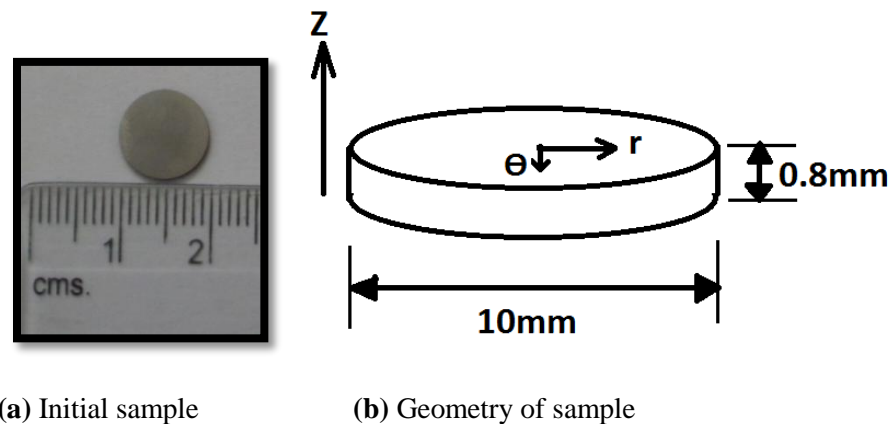


**Fig. 3.1:** Dimensions and schematic representation of the sample

#### 3.2 High Pressure Torsion Processing

High pressure torsion is carried out at Kyoto University in Prof. N. Tsuji's workshop on eight samples at constant pressure of 6 GPa and at constant load of 470 KN by rotating bottom anvil anticlockwise with the torque ranging from 5.4 to 7.4 Nm. Table below explains the working conditions as well as degree of rotation of bottom anvil during the HPT processing.

These samples are further characterized mechanically using micro-hardness tester at 0.5Hv and micro-structurally using EBSD analysis.



**Table 3.1** Processing conditions during HPT.

Rotations	Time	Force(KN)	Torque(Nm)
30 degree	25 sec	472	6.96
60 degree	50 sec	477	7.4
90 degree	1 min 15 sec	475	6.8
180 degree	2 min 31 sec	477	6.7
1 rotation	5 min 2 sec	465	6

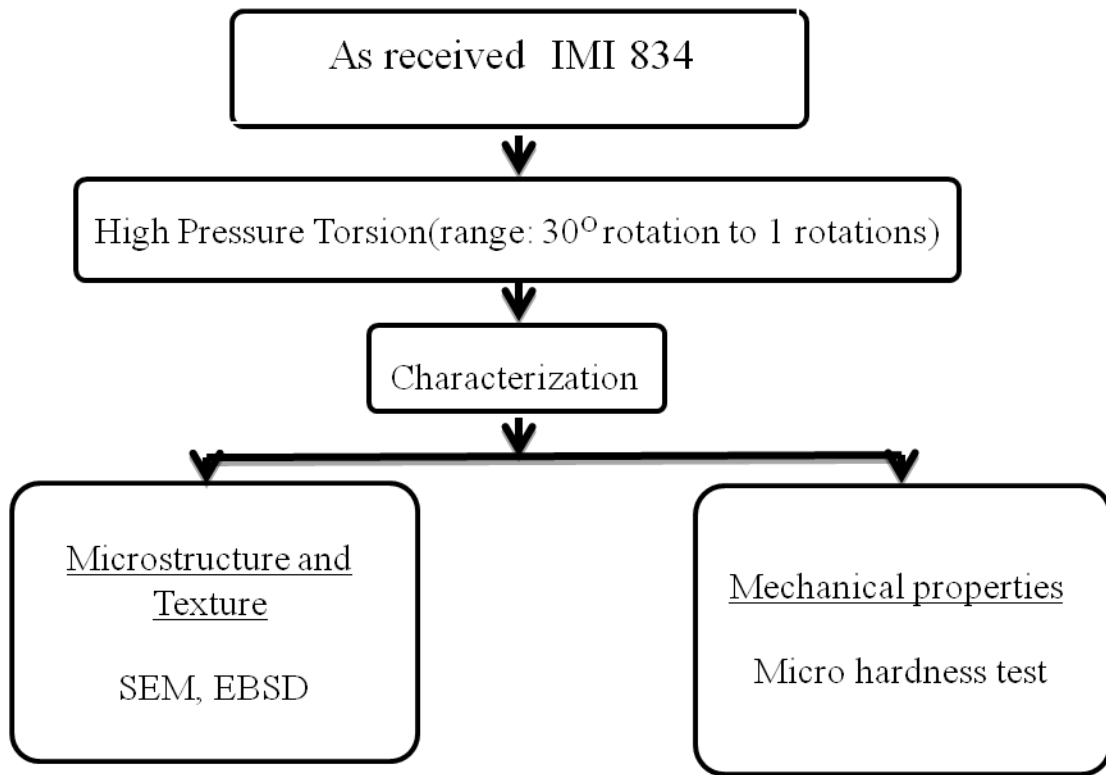


**Fig.3.2** Experimental flowchart

### 3.3 Characterization

#### 3.3.1 Hardness test on HPT processed disks

To measure the hardness variation across the disk, Vickers microhardness test (Make: EMCO-TEST, Austria; Model: Dura Scan-70) is conducted on the disks. The disks are hot mounted (Make: StruessCitupress- 10) and then manually ground and polished in order to obtain a mirror finish. To measure hardness variation precisely, microhardness indentation points are taken 0.5 mm apart from each other on two mutually perpendicular diameters of the disk under conditions of applied load of 500 g with a dwell time of 10 sec.

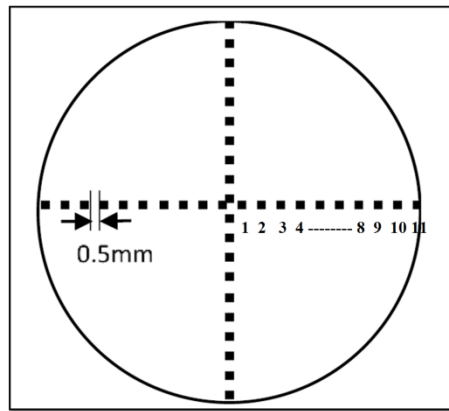
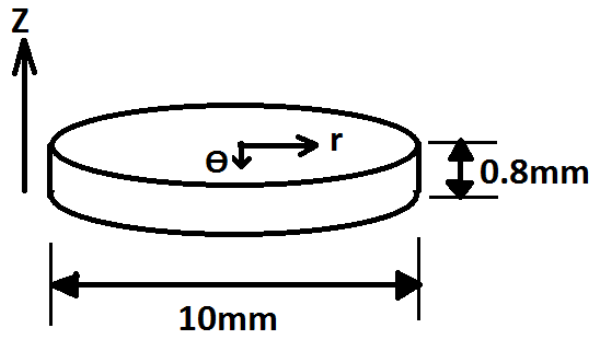


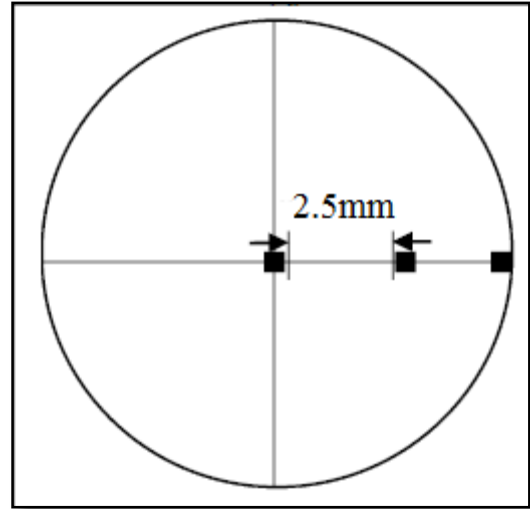
**Fig 3.3** Schematic illustration of microhardness measurements across the HPT disk.

#### 3.3.2 Microstructure and Texture Characterization

The microstructure and texture of the HPT processed disks are characterized by Electron Back Scattered Diffraction (EBSD) attached to a FEG-SEM (Make: Carl Zeiss; Model Supra 40) using Channel 5™ Software (Oxford Instruments, UK). EBSD measurements are taken on the  $r-\theta$  Plane of disks at center, middle and edge region of the disks as illustrated schematically in the Fig 3.4(b). For EBSD investigations, the samples are ground mechanically using SiC paper of grit size 2000, followed by electro-polishing using a A3 electrolyte (methanol, butyl alcohol, perchloric acid (6:3:1 volume fraction)) at 20V and 5°C (using liquid nitrogen) for 2 min for edge area and 5 min for center area. The microtexture analysis is performed by assuming triclinic sample symmetry.



(a)



(b)

Fig 3.4: Schematic illustration of (a) Sample geometry, (b) EBSD measurements areas.

## Chapter 4

### Results and Discussion

#### 4.1 HPT Processing

10 mm discs of IMI 834 alloy are HPT processed with rotations 30°, 60°, 90°, 180° and 1 complete rotation. Their camera images with corresponding strain values are given in Fig.4.1 and Table 4.1.

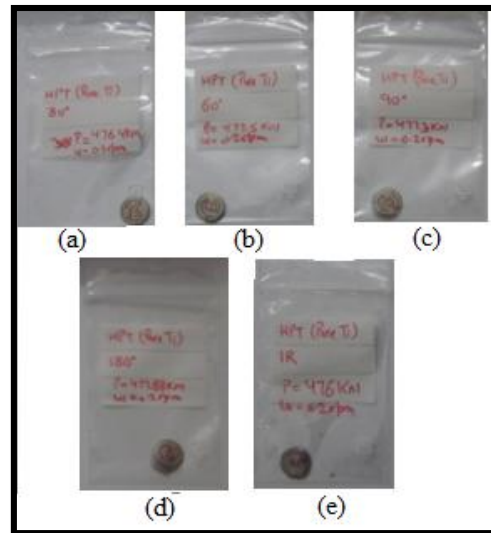


**Fig. 4.1** HPT processing of IMI-834 at (a) 30° (b) 60° (c) 90° (d) 180° (e) 1 rotation

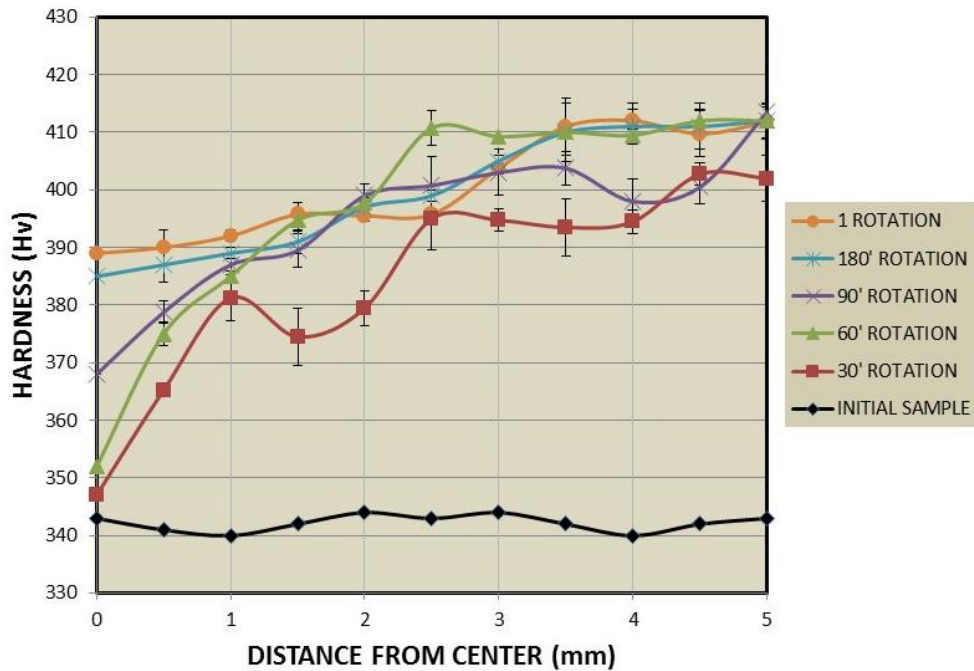
#### 4.2 Microhardness Properties

The distribution of hardness values across the diameters are shown in Fig. 4.2 for the disks processed by HPT, where “0” denotes the center of the specimen and 5 its edge. The hardness value for initial sample remained around 343 Hv. HPT increased the hardness values from center to the edge and with increased rotation values. The hardness values of the sample show very similar distribution behaviour by higher hardness values at the edge and minimum at the center which is typical for the HPT processed disks. Also, a plot of hardness with respect to strain value is given in Fig 4.3. This plot shows three stage hardness profile: first a steep increase in hardness up to strain value 0.65; second a small increase in hardness up to strain 2 and finally reaching a constant value of 414 Hv from strain value 2 till 4. Lowering of hardness values at strain values 0.79, 1.4 and 2.98 signify softening behaviour of IMI 834 at these strains. This behaviour may have occurred due to dislocation annihilation and/or dynamic recovery process at higher strains and can be best understood through orientation image mapping obtained through EBSD.

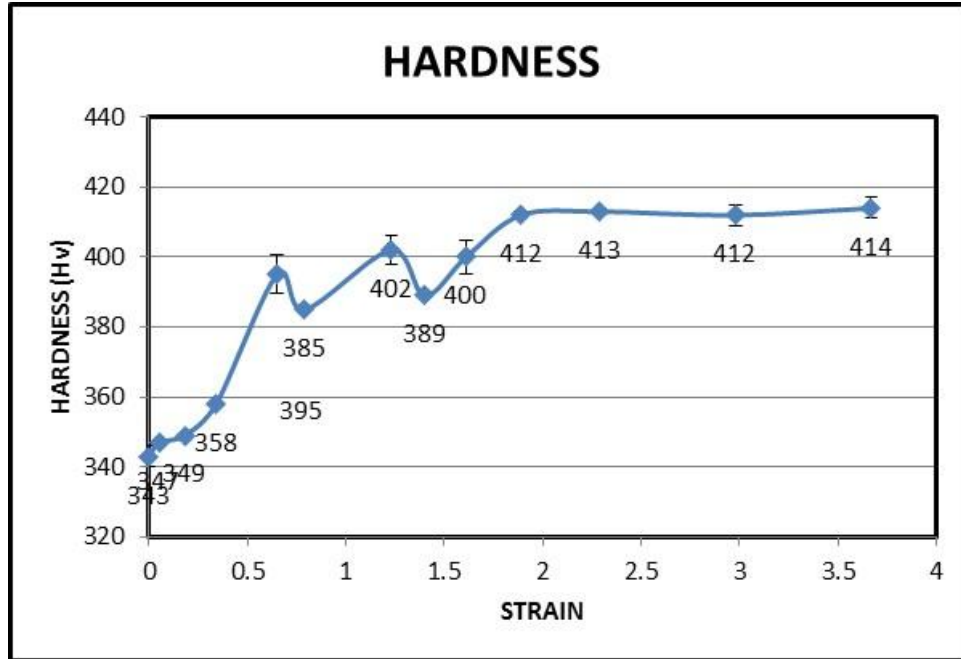
**Table 4.1** Strain values given with respect to the position along the radius and rotation.

ROTATION	POSITION	STRAIN
30 DEGREE	CENTER	0.05
	MIDDLE	0.64
	EDGE	1.23
60 DEGREE	CENTER	0.18
	MIDDLE	1.23
	EDGE	1.89
90 DEGREE	CENTRE	0.33
	MIDDLE	1.61
	EDGE	2.28
180 DEGREE	CENTER	0.79
	MIDDLE	2.29
	EDGE	2.98
1 ROTATION	CENTRE	1.4
	MIDDLE	2.98
	EDGE	3.67

### HARDNESS PROFILE



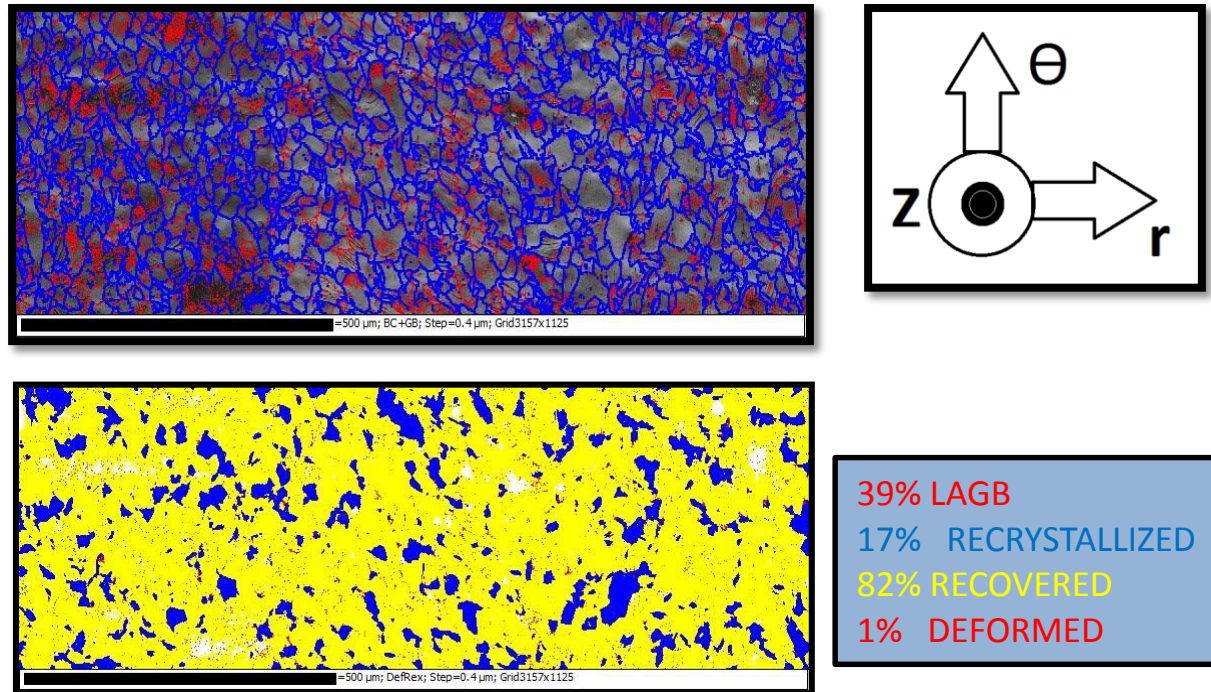
**Fig. 4.2** Hardness distribution in deformed specimens at different strain values.



**Fig 4.3** Hardness profile at different strains in IMI 834 alloy.

### 4.3 Microstructure Evolution

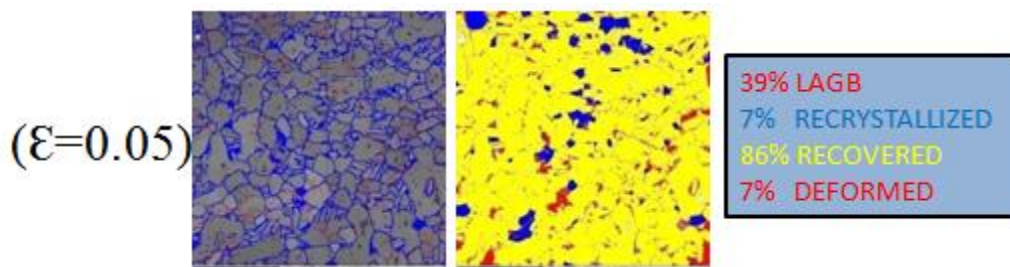
EBSD is used to obtain orientation image maps (OIMs) of the initial sample and HPT deformed specimens. Fig. 4.4 (a) shows the Kikuchi diffraction EBSD quality based OIM of IMI 834 starting material in  $r$ - $\theta$  plane. The high angle grain boundaries (HAGBs) having misorientation ( $> 15^\circ$ ) are marked in red colour and low angle grain boundaries (LAGBs) with misorientation (between  $2^\circ$  and  $15^\circ$ ) are highlighted in blue colour. The average grain size found is  $\sim 6 \mu\text{m}$  with fraction of HAGBs around 61%. Fig. 4.4 (b) shows OIM based on misorientation between neighbouring pixels and internal misorientation within the grain (a grain is defined having more than  $> 15^\circ$  misorientation). These neighbouring pixel misorientation is exploited as refining criteria of distinguishing grains as deformed (red coloured), recovered (yellow coloured) and recrystallized (blue coloured). The neighbouring pixel misorientation within a grain and having internal misorientation  $> 1^\circ$  is termed as deformed grain. Whereas, neighbouring pixel misorientation and overall internal misorientation in a grain  $< 1^\circ$  is termed as recrystallized grain. And the grain having neighbouring pixel misorientation  $< 1^\circ$  but overall internal misorientation  $> 1^\circ$  is termed as recovered grains. The as-received material microstructure reveals typical recovered/recrystallized microstructure (Fig. 4.4 (b)).



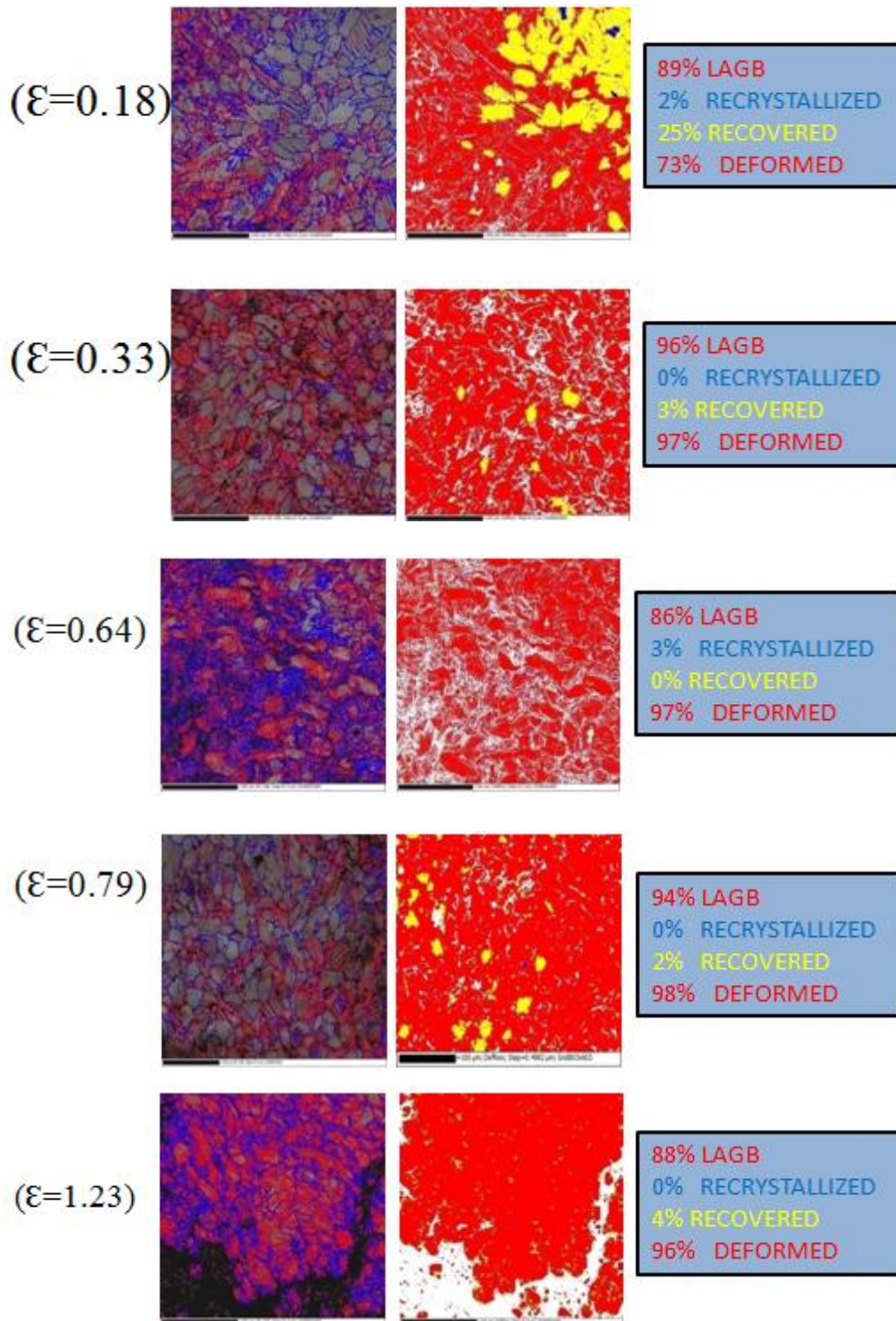
**Fig. 4.4 (a)** Kikuchi diffraction pattern based and **(b)** internal misorientation based OIMs of as-received sample.

Similar grain boundary with image quality and internal misorientation based OIMs are obtained for different strain values and are presented in Fig. 4.5 with respect to strain value. With increase in strain, increase in HAGB and deformed grain fraction can be noticed. Fig. 4.6 and Fig. 4.7 show volume fraction and grain size fraction of various type grains with respect to strain. The variation in the average grain size, deformation fraction and recovered fraction with imposed strain are plotted in Fig. 4.8.

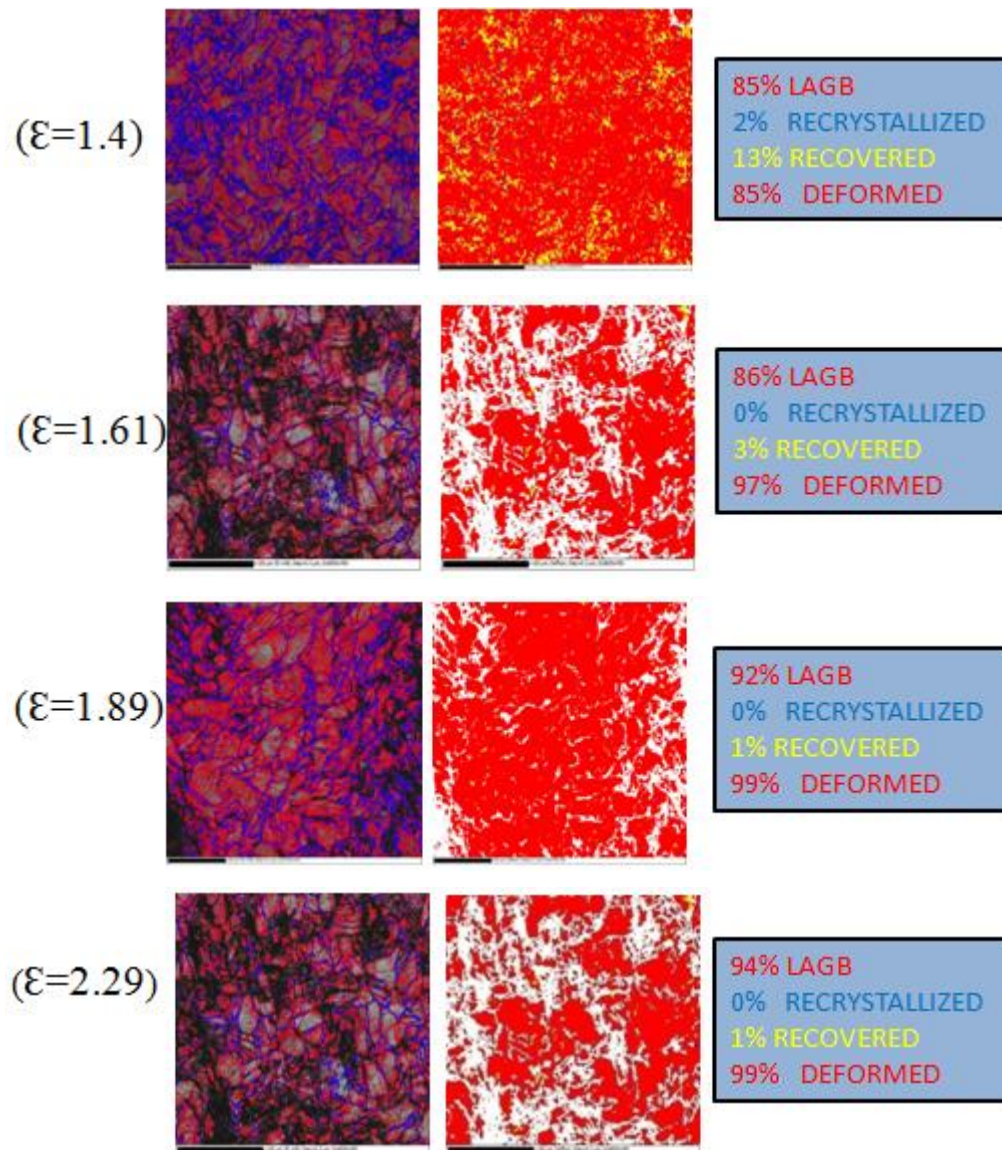
Fig 4.5 and Fig. 4.6 show severe deformation of IMI 834 with increase in strain followed by recovery at 1.4 and again deformation with strain and then recovery at  $\epsilon=2.98$ , creating a cycle of deformation and recovery stages. This cycle of deformation and recovery brings deviation in grain sizes (Fig. 4.7) generating ultrafine grain ( $1.8 \mu\text{m}$  at  $\epsilon=1.23$ ) at fully deformed microstructure to increase in bimodal character ( $1.3 \mu\text{m}$  and  $4.7 \mu\text{m}$  at  $\epsilon=2.98$ ) at the recovery stage.











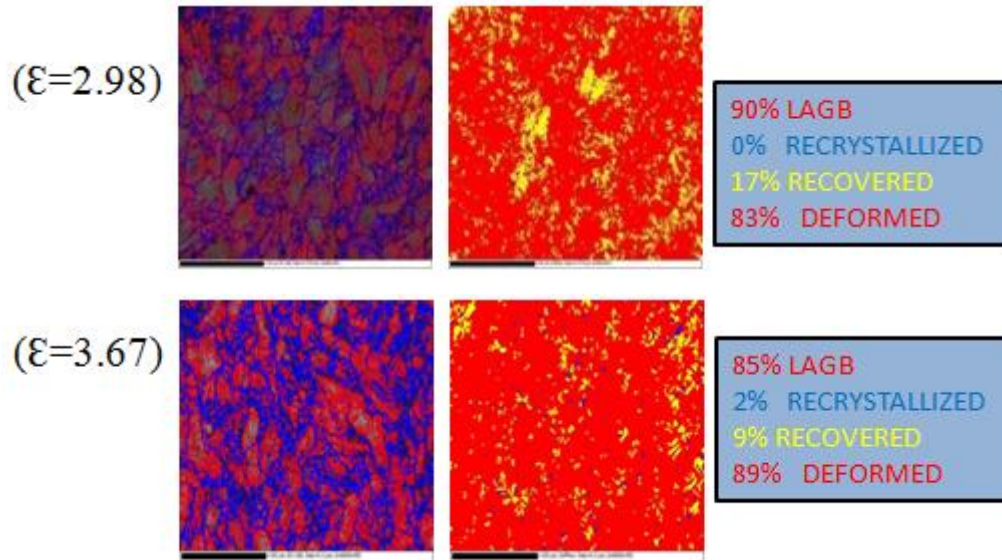


Fig 4.5 (a) Kikuchi diffraction pattern based and (b) internal misorientation based OIMs with respect to strain. White regions are non-indexed.

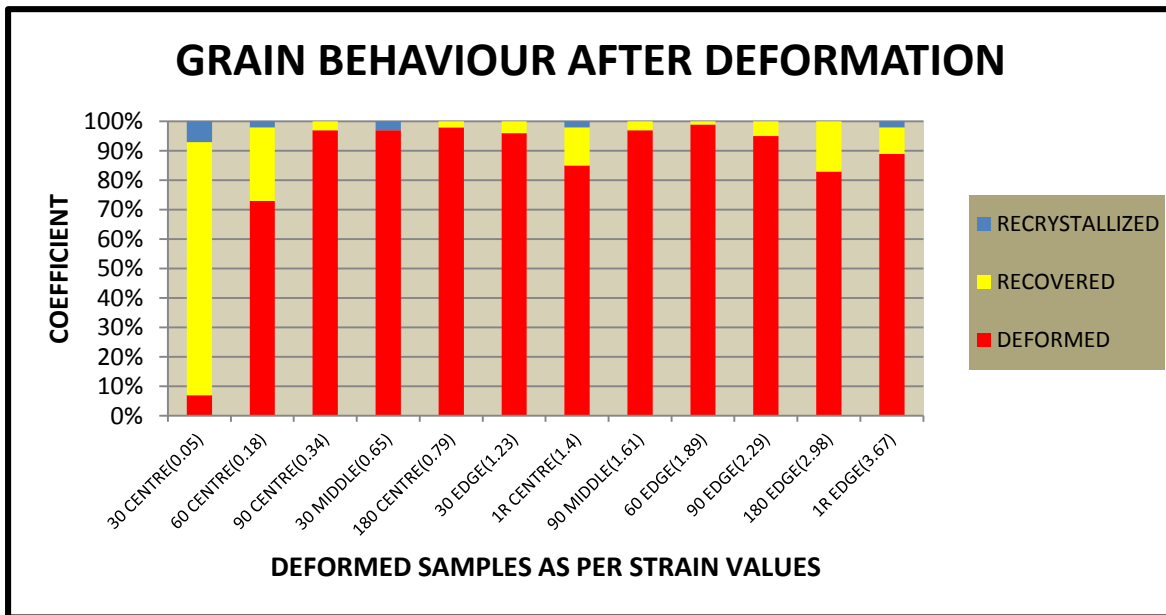
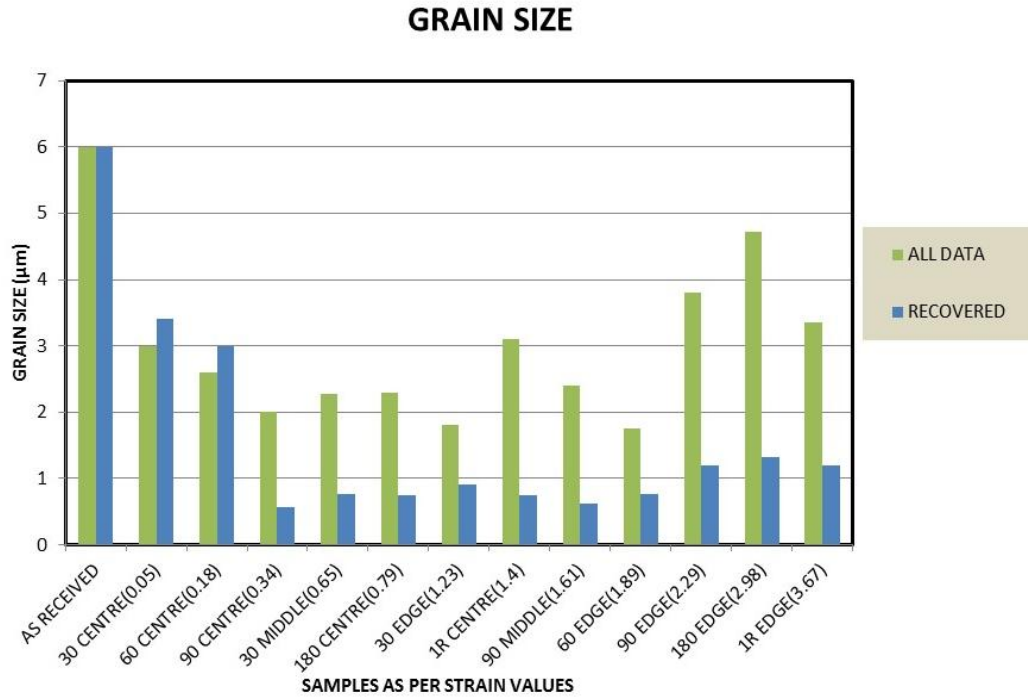


Fig 4.6 Variation in deformed, recovered and recrystallization fraction with respect to strain.



**Fig. 4.7** Grain size profile of sample with deformed and recovered grains.

Fig 4.8 shows the combined graph of grain types' volume fraction, total average grain size and LAGB fraction with respect to strain. There can be seen reduction in LAGB fraction at  $\epsilon = 0.79, 1.4$  and near  $2.98$ . Similar reduction trend can be found with volume fraction of deformed grains and accordingly increase in average grain size of all types of grains at similar strain values. This points towards stress/strain relaxation from severe plastic deformation in IMI 834 alloy at these strain values through low angle dislocation annihilation (at  $\epsilon=0.79$ ) and dynamic recovery (at  $\epsilon=1.4$  and  $2.98$ ). Incidentally, similar cycle of ups and downs (down at  $\epsilon= 0.79, 1.4$  and  $2.98$ ) is noticed in hardness profile as well (Fig. 4.3) and corroborate with the above stated phenomena.

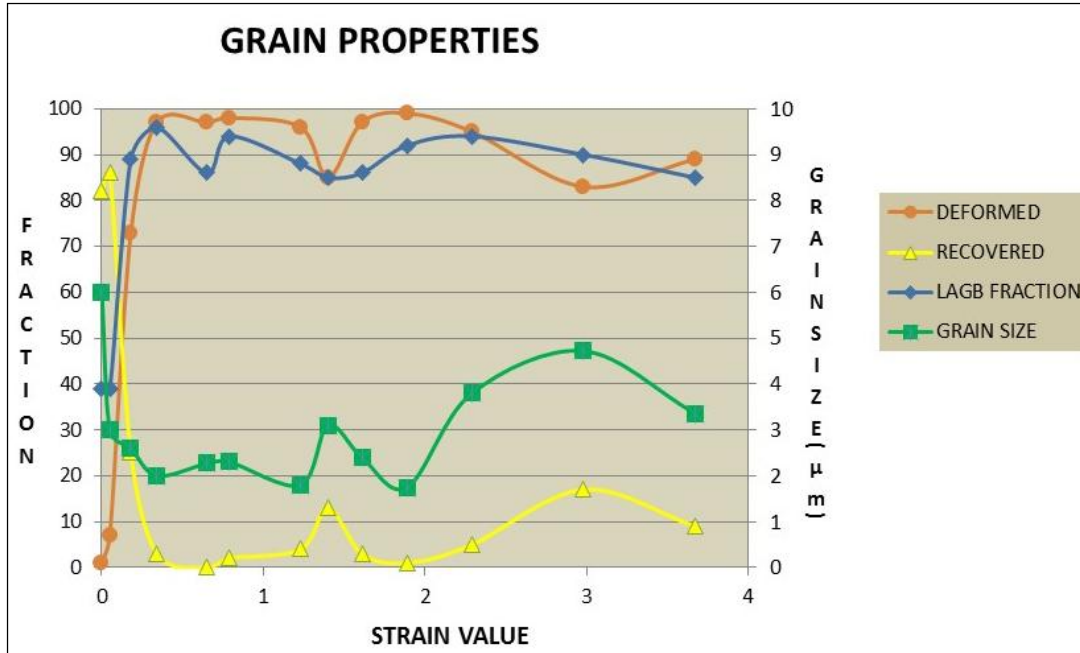


Fig. 4.8 Variation of deformation, recovery, LAGB fraction and grain size with strain.

#### 4.4 Micro-Texture Evolution

The standard HCP torsion pole figures are given in Fig. 4.9. Pole figures are obtained from the above stated OIMs and are represented through  $(0002)$  and  $\{10\bar{1}0\}$  pole figures of as-received and HPT deformed samples with their torsion texture components details in 4.10 to 4.21.

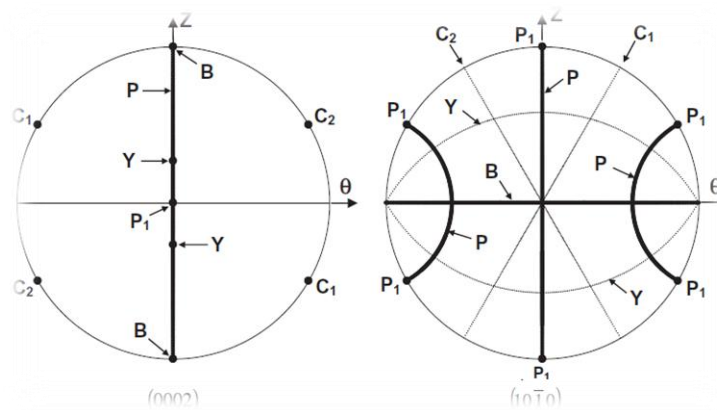
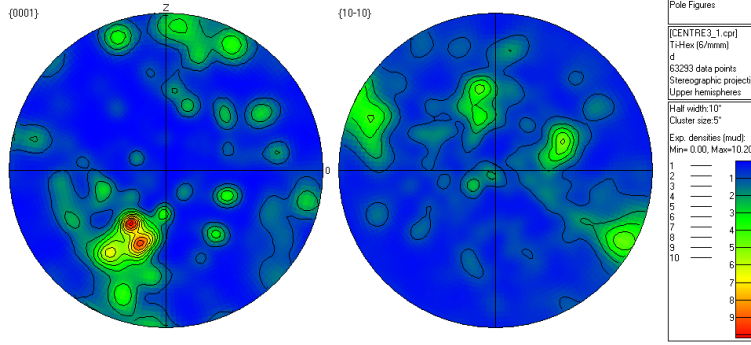
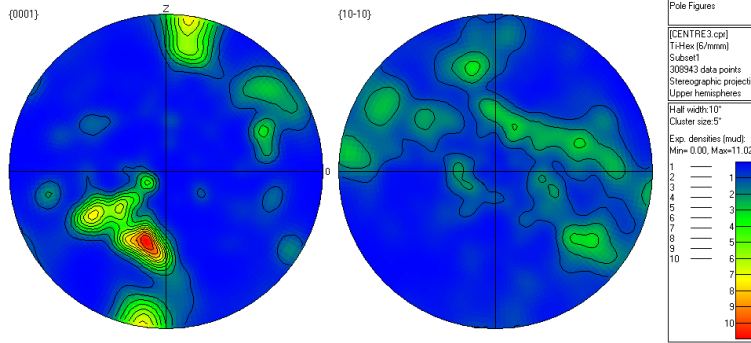


Fig 4.9 Standard torsion texture for HCP metals.



**Fig 4.10** Pole figures at  $\epsilon=0.05$  in z- $\theta$  plane.

STRAIN	TEXTURE COMPONENTS	ROTATION	SLIP SYSTEMS		
			SLIP DIRECTION( $\theta$ )	SLIP PLANE(Z)	TYPE
0.05	B,Y	-----	$\langle 11\bar{2}0 \rangle$	{0001} {11 $\bar{0}0$ } or {101 $\bar{0}$ }	A



**Fig 4.11** Pole figures at  $\epsilon=0.18$  in z- $\theta$  plane.

0.18	B,Y	Y(15°) AROUND $\langle 101\bar{0} \rangle$	$\langle 11\bar{2}0 \rangle$	{0001} {11 $\bar{0}0$ } or {101 $\bar{0}$ }	c+a
------	-----	-----------------------------------------------	------------------------------	------------------------------------------------	-----

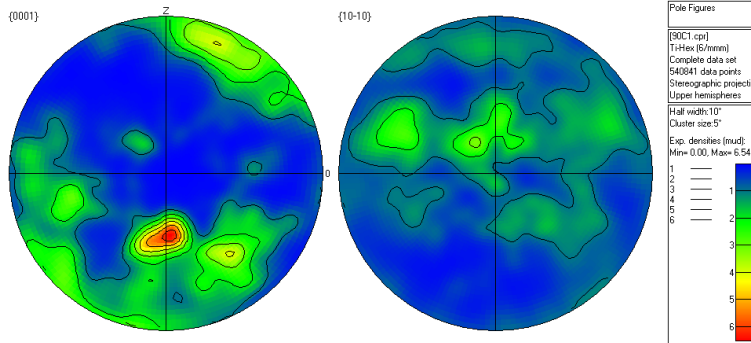


**Fig 4.12** Pole figures at  $\epsilon=0.34$  in z- $\theta$  plane.



0.34	Y,B,C	B,Y(10°) AROUND <101 $\bar{0}$ >	<11 $\bar{2}0$ >	{0001} {11 $\bar{0}0$ } or {101 $\bar{0}$ }	a
			<11 $\bar{2}3$ >	{10 $\bar{1}1$ } or {11 $\bar{2}2$ }	c+a

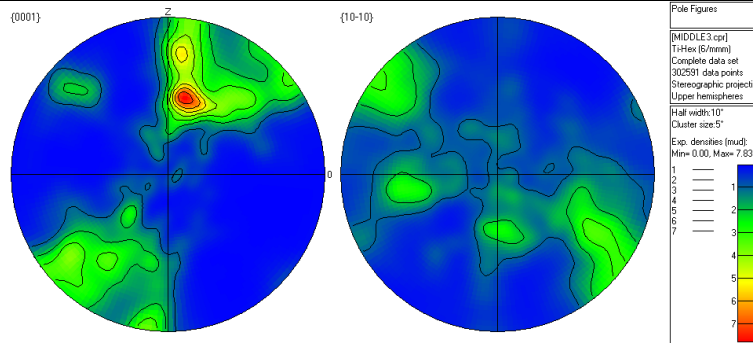


Fig 4.13 Pole figures at  $\epsilon=0.65$  in z- $\theta$  plane.

0.65	Y->B,C	Y,C(10°) AROUND <101 $\bar{0}$ >	<11 $\bar{2}3$ >	{0001} {11 $\bar{0}0$ } or {101 $\bar{0}$ }	a
			<11 $\bar{2}0$ >	{10 $\bar{1}1$ } or {11 $\bar{2}2$ }	c+a

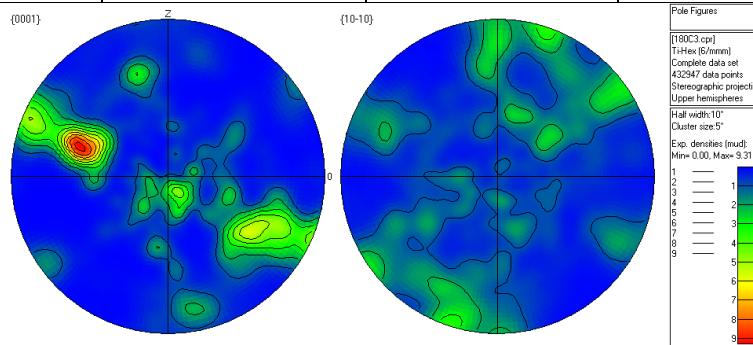


Fig 4.14 Pole figures at  $\epsilon=0.79$  in z- $\theta$  plane.

0.79	C,P1	C(30°) AROUND <101 $\bar{0}$ >	<11 $\bar{2}3$ >	{10 $\bar{1}1$ } or {11 $\bar{2}2$ }	c+a
			<11 $\bar{2}0$ >	{11 $\bar{0}0$ } or {101 $\bar{0}$ }	a

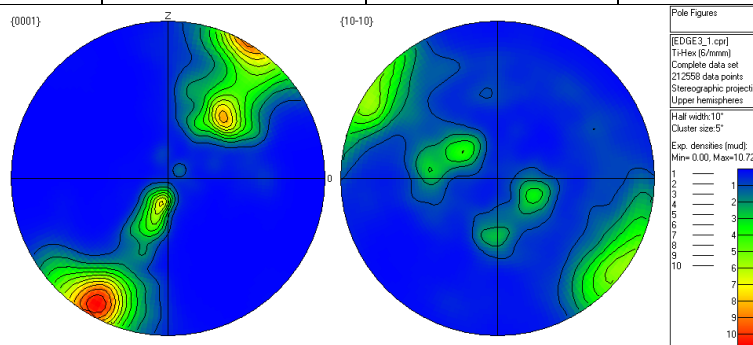


Fig 4.15 Pole figures at  $\epsilon=1.23$  in z- $\theta$  plane.

1.23	C,P1	C,P1(30°) AROUND <1010̄>	<112̄3>	{101̄1} or {112̄2}	c+a
			<112̄0>	{110̄0} or {1010̄}	a

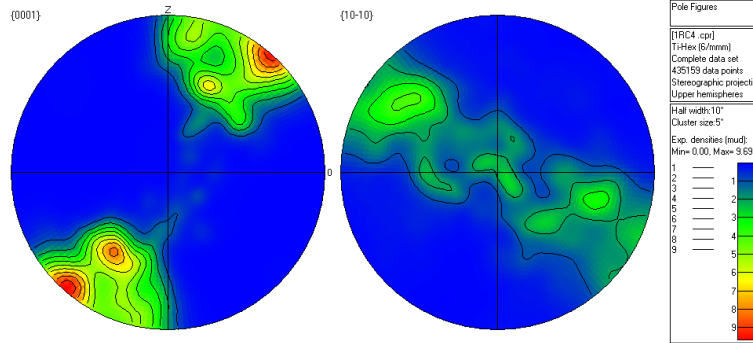


Fig 4.16 Pole figures at  $\epsilon=1.4$  in z- $\theta$  plane.

1.4	C,B	C(30°) AROUND <1010̄>	<112̄3>	{101̄1} or {112̄2}	c+a
			<112̄0>	{0001}	a

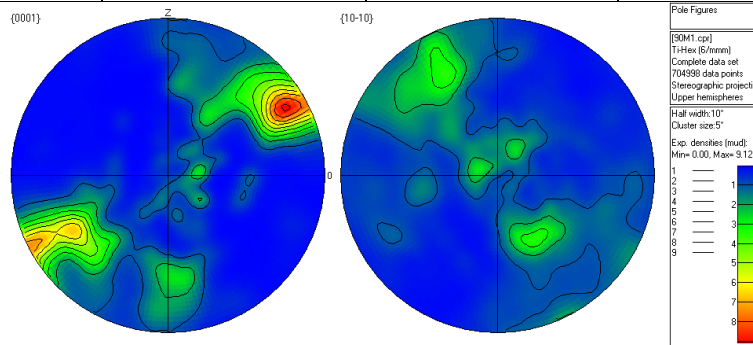


Fig 4.17 Pole figures at  $\epsilon=1.61$  in z- $\theta$  plane.

1.61	C,B->Y	C(20°) AROUND <1010̄>	<112̄3>	{101̄1} or {112̄2}	c+a
			<112̄0>	{0001} {110̄0} or {1010̄}	a

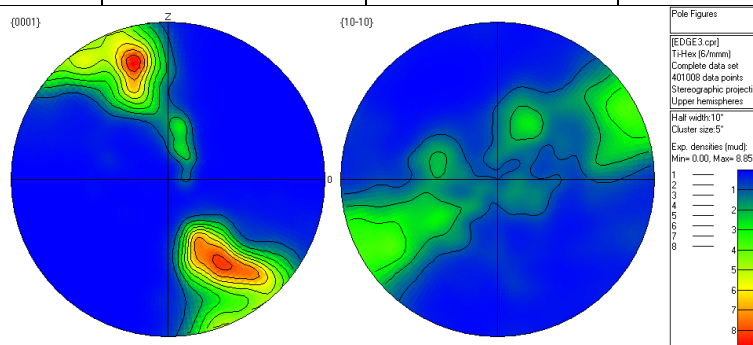


Fig 4.18 Pole figures at  $\epsilon=1.84$  in z- $\theta$  plane.

1.84	C,B->Y	C(30°) AROUND <1010̄>	<1123̄>	{101̄1} or {112̄2}	c+a
			<1120̄>	{0001} {110̄0} or {1010̄}	a

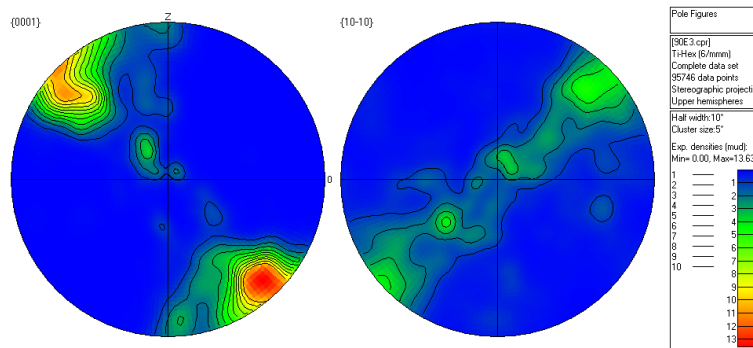


Fig 4.19 Pole figures at  $\epsilon=2.29$  in z- $\theta$  plane.

2.29	C,B,P1	C(10°) AROUND <1010̄>	<1123̄>	{101̄1} or {112̄2}	c+a
			<1120̄>	{0001} {110̄0} or {1010̄}	a

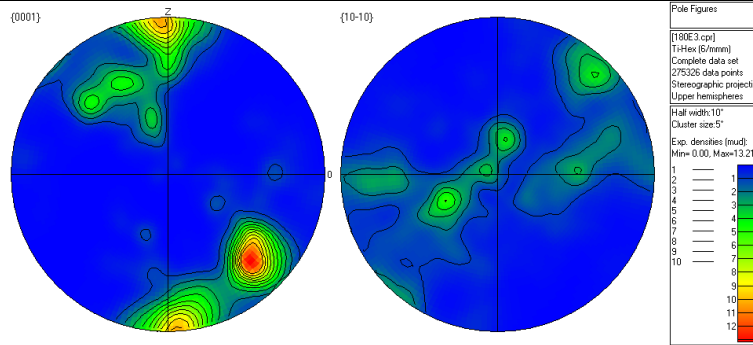
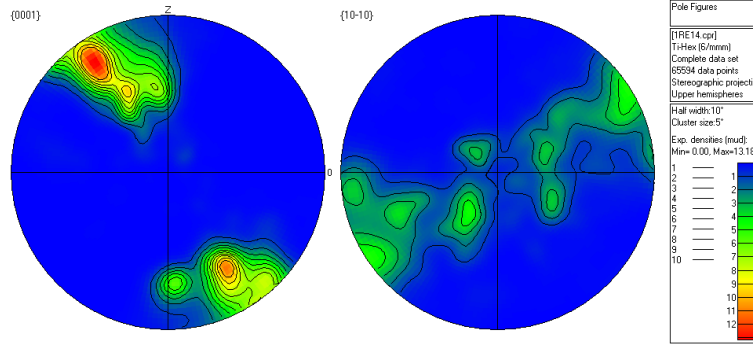


Fig 4.20 Pole figures at  $\epsilon=2.98$  in z- $\theta$  plane.

2.98	C,B(STRONG)->Y	----	<1123̄>	{101̄1} or {112̄2}	c+a
			<1120̄>	{0001} {110̄0} or {1010̄}	a





**Fig 4.21** Pole figures at  $\epsilon=3.67$  in  $z-\theta$  plane.

3.67	C,B->Y	C(20°) AROUND <101 $\bar{0}$ >	<11 $\bar{2}$ 3>	{10 $\bar{1}$ 1} or {11 $\bar{2}$ 2}	c+a
			<11 $\bar{2}$ 0>	{0001} {1 $\bar{1}$ 00} or {10 $\bar{1}$ 0}	a

A compiled data table containing the texture components with their associated crystallographic slip systems of all strain is given in Table 4.2.

Low strain values ( $\epsilon=0.05$  and  $0.18$ ) initiates  $\langle a \rangle$  direction shear (along  $\theta$ ) on basal, pyramidal and prismatic planes generating B and partial P (up to Y) fibres. Increasing strain values ( $\epsilon=0.34$  onwards) in addition to shear along  $\langle a \rangle$  direction also activated shear along  $\langle c+a \rangle$  i.e.  $\langle 11\bar{2}3 \rangle \parallel \theta$  direction on pyramidal type I and type II planes creating C fibre and movement of B towards P1 via Y happened through shear along  $\theta \parallel \langle 11\bar{2}0 \rangle$ . C fibre gained maximum fraction from strain  $0.79$  onwards stating  $\langle c+a \rangle$  shear on pyramidal type I and type II planes gaining more dominance over the  $\langle a \rangle$  shear on basal, pyramidal and prismatic planes.

Also, increased strain showed rotation of the standard texture component (mainly C) up to  $30^\circ$  along  $\langle 10\bar{1}0 \rangle$  axis. Rotations around  $[0002]$  by  $30^\circ$  and  $\langle 10\bar{1}0 \rangle$  by  $90^\circ$  are reported during dynamic recrystallization of HCP metals [23]. But these rotations along  $\langle 10\bar{1}0 \rangle$  axis during severe deformation are might be combined  $\langle a \rangle$  and  $\langle c+a \rangle$  shear effects.

Furthermore, the dynamic recovered strain microstructures (at  $\epsilon=1.4$  and  $2.98$ ) showed the reappearance of B fibre (Fig. 4.16 and Fig. 4.20) stating the recovered grains are basal oriented i.e.  $(0002)\langle 11\bar{2}0 \rangle$ .

Hence, the domination of prismatic and pyramidal slip systems at higher strain and the frequent reoccurrences of basal plane shear also confirms the cycles of deformation-recovery during HPT of IMI 834 alloy.

**Table 4.2** HPT texture components of IMI 834 with their crystallographic slip details at different strain values.

STRAIN	TEXTURE COMPONENTS	ROTATION	SLIP SYSTEMS		
			SLIP DIRECTION( $\Theta$ )	SLIP PLANE(Z)	TYPE
0.05	B,Y	-----	$\langle 11\bar{2}0 \rangle$	$\{0001\}$ $\{1\bar{1}00\}$ or $\{10\bar{1}0\}$	$\langle a \rangle$
0.18	B,Y	Y( $15^\circ$ ) AROUND $\langle 101\bar{0} \rangle$	$\langle 11\bar{2}0 \rangle$	$\{0001\}$ $\{1\bar{1}00\}$ or $\{10\bar{1}0\}$	$\langle a \rangle$
0.34	Y,B,C	B,Y( $10^\circ$ ) AROUND $\langle 101\bar{0} \rangle$	$\langle 11\bar{2}0 \rangle$	$\{0001\}$ $\{1\bar{1}00\}$ or $\{10\bar{1}0\}$	$\langle a \rangle$
			$\langle 11\bar{2}3 \rangle$	$\{10\bar{1}1\}$ or $\{11\bar{2}2\}$	$\langle c+a \rangle$
0.65	Y->B,C	Y,C( $10^\circ$ ) AROUND $\langle 101\bar{0} \rangle$	$\langle 11\bar{2}0 \rangle$	$\{0001\}$ $\{1\bar{1}00\}$ or $\{10\bar{1}0\}$	$\langle a \rangle$
			$\langle 11\bar{2}3 \rangle$	$\{10\bar{1}1\}$ or $\{11\bar{2}2\}$	$\langle c+a \rangle$
0.79	C,P1	C( $30^\circ$ ) AROUND $\langle 101\bar{0} \rangle$	$\langle 11\bar{2}3 \rangle$	$\{10\bar{1}1\}$ or $\{11\bar{2}2\}$	$\langle c+a \rangle$
			$\langle 11\bar{2}0 \rangle$	$\{1\bar{1}00\}$ or $\{10\bar{1}0\}$	$\langle a \rangle$
1.23	C,P1	C,P1( $30^\circ$ ) AROUND $\langle 101\bar{0} \rangle$	$\langle 11\bar{2}3 \rangle$	$\{10\bar{1}1\}$ or $\{11\bar{2}2\}$	$\langle c+a \rangle$
			$\langle 11\bar{2}0 \rangle$	$\{1\bar{1}00\}$ or $\{10\bar{1}0\}$	$\langle a \rangle$
1.4	C,B	C( $30^\circ$ ) AROUND $\langle 101\bar{0} \rangle$	$\langle 11\bar{2}3 \rangle$	$\{10\bar{1}1\}$ or $\{11\bar{2}2\}$	$\langle c+a \rangle$
			$\langle 11\bar{2}0 \rangle$	$\{0001\}$	$\langle a \rangle$
1.61	C,B->Y	C( $20^\circ$ ) AROUND $\langle 101\bar{0} \rangle$	$\langle 11\bar{2}3 \rangle$	$\{10\bar{1}1\}$ or $\{11\bar{2}2\}$	$\langle c+a \rangle$
			$\langle 11\bar{2}0 \rangle$	$\{0001\}$ $\{1\bar{1}00\}$ or $\{10\bar{1}0\}$	$\langle a \rangle$
1.84	C,B->Y	C( $30^\circ$ ) AROUND $\langle 101\bar{0} \rangle$	$\langle 11\bar{2}3 \rangle$	$\{10\bar{1}1\}$ or $\{11\bar{2}2\}$	$\langle c+a \rangle$
			$\langle 11\bar{2}0 \rangle$	$\{0001\}$ $\{1\bar{1}00\}$ or $\{10\bar{1}0\}$	$\langle a \rangle$
2.29	C,B,P1	C( $10^\circ$ ) AROUND $\langle 101\bar{0} \rangle$	$\langle 11\bar{2}3 \rangle$	$\{10\bar{1}1\}$ or $\{11\bar{2}2\}$	$\langle c+a \rangle$
			$\langle 11\bar{2}0 \rangle$	$\{0001\}$ $\{1\bar{1}00\}$ or $\{10\bar{1}0\}$	$\langle a \rangle$
2.98	C,B(STRONG)->Y	-----	$\langle 11\bar{2}3 \rangle$	$\{10\bar{1}1\}$ or $\{11\bar{2}2\}$	$\langle c+a \rangle$
			$\langle 11\bar{2}0 \rangle$	$\{0001\}$ $\{1\bar{1}00\}$ or $\{10\bar{1}0\}$	$\langle a \rangle$
3.67	C,B->Y	C( $20^\circ$ ) AROUND $\langle 101\bar{0} \rangle$	$\langle 11\bar{2}3 \rangle$	$\{10\bar{1}1\}$ or $\{11\bar{2}2\}$	$\langle c+a \rangle$
			$\langle 11\bar{2}0 \rangle$	$\{0001\}$ $\{1\bar{1}00\}$ or $\{10\bar{1}0\}$	$\langle a \rangle$

## Chapter 5

### Conclusions

- High pressure torsion (HPT), a severe plastic deformation technique, of various rotations are performed on IMI 834 alloy (a near  $\alpha$  titanium alloy) 10 mm diameter discs to study its effect on  $\alpha$  phase.
- Hardness profiling from center towards the edge of the disc of various rotations shows hardening with increase in rotation, before finally reaching a saturation. At strains ( $\epsilon=0.79, 1.4$  and  $2.98$ ) softening with decreased hardness value is noticed.
- From microstructure orientation image map (OIMs), comprehensive microstructure-texture details are obtained. The fraction of deformed grains increases with strain but with appearances of recovered fraction at strains  $\epsilon=1.4$  and  $2.98$  indicating dynamic recovery. Also the decrease of low angle grain boundary fraction at  $\epsilon=0.79$  point towards dislocation annihilation at initial straining. This indicates occurrence of cycles of deformation-recovery during HPT.
- The deformation and recovery cycles reduced the initial material grain size ( $6 \mu\text{m}$ ) to ultrafine grain ( $1.8 \mu\text{m}$  at  $\epsilon=1.23$ ) at the fully deformed microstructure and to bimodal character ( $1.3 \mu\text{m}$  and  $4.7 \mu\text{m}$  at  $\epsilon=2.98$ ) at the recovery stage.
- Texture analyses through  $(0001)$  and  $\{10\bar{1}0\}$  pole figures show activation of shear along  $\langle a \rangle$  ( $\langle 11\bar{2}0 \rangle$ ) direction in basal, pyramidal and prismatic planes during initial straining ( $\epsilon=0.05$  and  $0.18$ ) generating B and partial P (up to Y) fibres. Further strains ( $\epsilon=0.34$  onwards) increased participation of  $\langle c+a \rangle$  ( $\langle 11\bar{2}3 \rangle$ ) shear producing C fibre along with shear along  $\langle a \rangle$  generating movement of B towards P1 via Y.
- Increased strain showed rotation of the standard texture component (mainly C) up to  $30^\circ$  along  $\langle 10\bar{1}0 \rangle$  axis which might be a combined  $\langle a \rangle$  and  $\langle c+a \rangle$  shear effect.
- Dynamic recovered strain microstructures (at  $\epsilon=1.4$  and  $2.98$ ) showed the reappearance of B fibre stating the basal orientation i.e.  $(0001)\langle 11\bar{2}0 \rangle$  of the recovered grains. This also confirms the occurrence of deformation-recovery cycle during HPT of IMI 834 alloy.

## References

1. Titanium second edition by GerdLütjering James C. Williams.
2. R.R Boyer, An overview of the use of titanium in the aerospace industry, *Materials science and Engineering A213* (1996) 103-114.
3. D.F.Neal,in G. Lutjering, U. Zwicker and W.Bunk (eds.),*Optimisation of creep and fatigue resistance in high temperature Ti alloys IMI829 and IMI 834*,Titanium Science and Technology, Deutsche Gesellschaft fur Metallkunde.V., Oberursl, Germany, 1985, pp. 2419-2424.
4. D.F. Neal, in P. Lacombe, R.Tricot and G. Beranger (eds.), *Development and evaluation on high temperature titanium alloy IMI 834*, Sixth world Conference on Titanium, SocieteFrancaise de Metallurgie, Cedex, France, 1989, pp. 253-258.
5. D.F Neal in *Titanium Science and Technology*, G.Lutjering, U. Zwiicker and W. Bunk, eds, Deutsche Gesellschaft fur Metallkunde e-U obseruses, Germany, 1985, pp. 2419-24
6. P.A. Blenkinsopp: in *Titanium'92 Science and Technology*, F.H. Frous and I.Caolan, eds., TMS, warrendale PA, 1993, PP. 15-26.
7. R.R Boyer. *Mater. Sci. Eng. A*; 1996, vol. 213 A PP. 103-14.
8. M.R Bacher, *Int.J.Fatigue* 25(2003)1079-1087.
9. X.WANG, P.VO, M.JAHAZI, and S.YUE, *Metallurgical and materials transactions A*, volume 38A, April 2007-839.
10. G.A. Salishchev, O.R. Valiakhmetov, and R.M. Galeyev: *J. Mater.Sci.*, 1993, vol. 28, pp. 2898-2902.
11. M.F.X. Gigliotti, B.P. Bewlay, J.B. Daton, R.S. Gilmore and G.A. Salishchev. *Metallurgical and materials transactions A*, volume 31A, September 2000—2119.
12. Erb U, El-Sherik AM, Palumbo G, Aust KT, *Synthesis, structure and properties of electroplated nanocrystalline materials. Nanostructured Materials*, 1993. 2: p. 383-390.
13. Gleiter H. In: Hansen N, Horsewell A, Leffers T, Lilholt H, editors, *Deformation of polycrystals: Mechanisms and microstructures*. Roskilde, Denmark: Riso National Laboratory, 1981: p. 15
14. Koch CC, Cho YS., *Nanocrystals by high energy ball milling. Nanostruct Mater*, 1992. 2: p. 207-212
15. Ruslan Z. Valiev, Terence G. Langdon. *Principles of equal-channel angular pressing as a processing tool for grain refinement*, *Progress in Materials Science* 51 (2006) 881–981
16. R.Z. Valiev, R.K. Islamgaliev, I.V. Alexandrov, *Bulk nanostructured materials from severe plastic deformation. Progress in Materials Science*, 2000. 45(2): p. 103-189

17. Y. Saito, H. Utsunomiya, N. Tsuji, T. Sakai, Novel ultra-high straining process for bulk materials—development of the accumulative roll-bonding (ARB) process. *Acta Materialia*, 1999. 47(2): p. 579-583
18. A.P. Zhilyaev, T.G. Langdon, Using high-pressure torsion for metal processing. *Fundamentals and applications Progress in Materials Science*, 2008. 53(6): p. 893-979
19. Benoit Beausir, Laszlo S. Toth, Kenneth W. Neale, Ideal orientations and persistence characteristics of hexagonal close packed crystals in simple shear, *Acta Materialia* 55 (2007) 2695–2705
20. Ying Chun Wang, Terence G. Langdon, Influence of phase volume fractions on the processing of a Ti–6Al–4V alloy by high-pressure torsion, *Materials Science & Engineering A* 559(2013)861–867
21. Somjeet Biswas, Benoit Beausir, Laszlo S. Toth, Satyam Suwas, Evolution of texture and microstructure during hot torsion of a magnesium alloy, *Acta Materialia* 61 (2013) 5263–5277
22. A. Serra, D.J. Bacon, R.C. Pond, Twins as barriers to basal slip in hexagonal-closed-packed metals, *Metallurgical and Materials Transactions A*, 33A, March 2002, p 809.
23. Ruslan Z. Valiev, Terence G. Langdon, Principles of equal-channel angular pressing as a processing tool for grain refinement, *Progress in Materials Science* 51 (2006) 881–981.